than 15 min to allow for physical decay of O-15 radioactivity to background levels. All acquisitions were obtained in the two-dimensional mode (septa extended).

Data analysis

A filtered back-projection algorithm with a 6-mm Gaussian filter was used for image reconstruction. The reconstructed images had a matrix size of 128 × 128 × 47 and a voxel size of 1.84 × 1.84 × 3.38 mm, and all image data sets were resliced into short-axis images across the left ventricle [13].

Myocardial blood flow

rMBF was calculated from the injection of ^{15}O-H_2O by fitting the myocardial and arterial time-activity curve data to a single-tissue-compartment model that implemented corrections for partial-volume effects by introducing the tissue fraction. In addition, the model was corrected for spillover from the left ventricular (LV) chamber into the myocardial ROI by introducing the arterial blood volume [13]. In these experiments, the time-activity curves generated from large ROIs placed in the LV chamber were used as the input function.

Regional oxygen extraction fraction

In the "injection" study, rOEF was calculated according to Eqs. (2) and (5). In these formulations, F_{vein} was assumed to be 0.10 ml/g tissue and p was fixed at 0.90 ml/g. The blood volume image obtained from the ^{15}O-CO scan was used for the determination of V_B^{myo}. The value of $A_t(t)$ was obtained from the LV radioactivity concentration measured from the PET data set with small LV ROIs to minimize spillover from the myocardium. The calculation for the estimation of recirculating ^{15}O-H_2O was performed as previously described [16]. For the "continuous infusion" and "continuous inhalation" studies, in which a 600-s frame was regarded as steady-state, Eqs. (3) and (5) or Eqs. (3) and (4) were used for calculating rOEF, respectively.

Results

Table 1 summarizes the conditions of animals during the PET studies. The parameters were all within the physiologic range.

Figure 2 demonstrates the dynamic images obtained in the "injection", "continuous infusion", and "continuous inhalation" studies. With the injection and continuous-infusion methods, the right ventricle on the left side and the vena cava on the lower side were well delineated, whereas the left ventricle was moderately shown on the right side. The 16th frame (600~1,200 s after the initiation), which was used for steady-state analysis with the continuous-infusion method, was visibly distinct compared with all of the frames obtained with the injection method. However, with the continuous-inhalation method, neither ventricle could be depicted because of high radioactivity in the lung on the right and lower-side images.

The radioactivity in the blood pool obtained by ^{15}O-CO PET (Fig. 3g) and the gaseous volume estimated by inverse transmission data (Fig. 3h) were subtracted from the raw PET images (16th frame) with the continuous-inhalation and continuous-infusion methods, respectively (Fig. 3c and f). Both methods clearly delineated the myocardium after subtraction in comparison to the blood flow image (Fig. 3i). However, the continuous-inhalation method showed salient radioactivity on the lateral wall (Fig. 3c), whereas the continuous-infusion method showed only modest radioactivity in the myocardium (Fig. 3f). It is also notable that there was considerable radioactivity in the right ventricle with the continuous-infusion method even after the subtraction (Fig. 3f).

To further examine the differences between the continuous-infusion and continuous-inhalation methods, time-radioactivity curves during the PET scans were taken from four ROIs: the left ventricle (LV), right ventricle (RV), myocardium (Myo), and lung (Fig. 4). At the steady-state frame (600~1,200 s), the continuous-infusion method showed higher radioactivity in the RV and LV than in the myocardium (Fig. 4a), whereas the radioactivity of these regions was similar with the continuous-inhalation method (Fig. 4b). The radioactivity in LV was about two-thirds of that in RV in Fig. 4a, indicating that measurable radioactivity was excreted through the lung even after the femoral administration of ^{15}O-O_2. The lung excretion was also observed on the blood-subtracted image (Fig. 3e). Actually, there was significant radioactivity in the lung (Fig. 4a), although that was the lowest among the four ROIs. In contrast, the radioactivity in the myocardium was the lowest among the four ROIs with the continuous-inhalation method

Table 1 Physiological parameters of pigs during the PET studies

	pH	pCO_2 (mmHg)	pO_2 (mmHg)	tHb (g/dl)	O_2Sat (%)	HR (bpm)	BP (mmHg)	
							Diastolic	Systolic
Average	7.46	40.3	125.8	12.8	97.7	85	97.8	125.2
SD	0.032	2.51	16.69	1.30	1.83	19.5	10.4	19.3

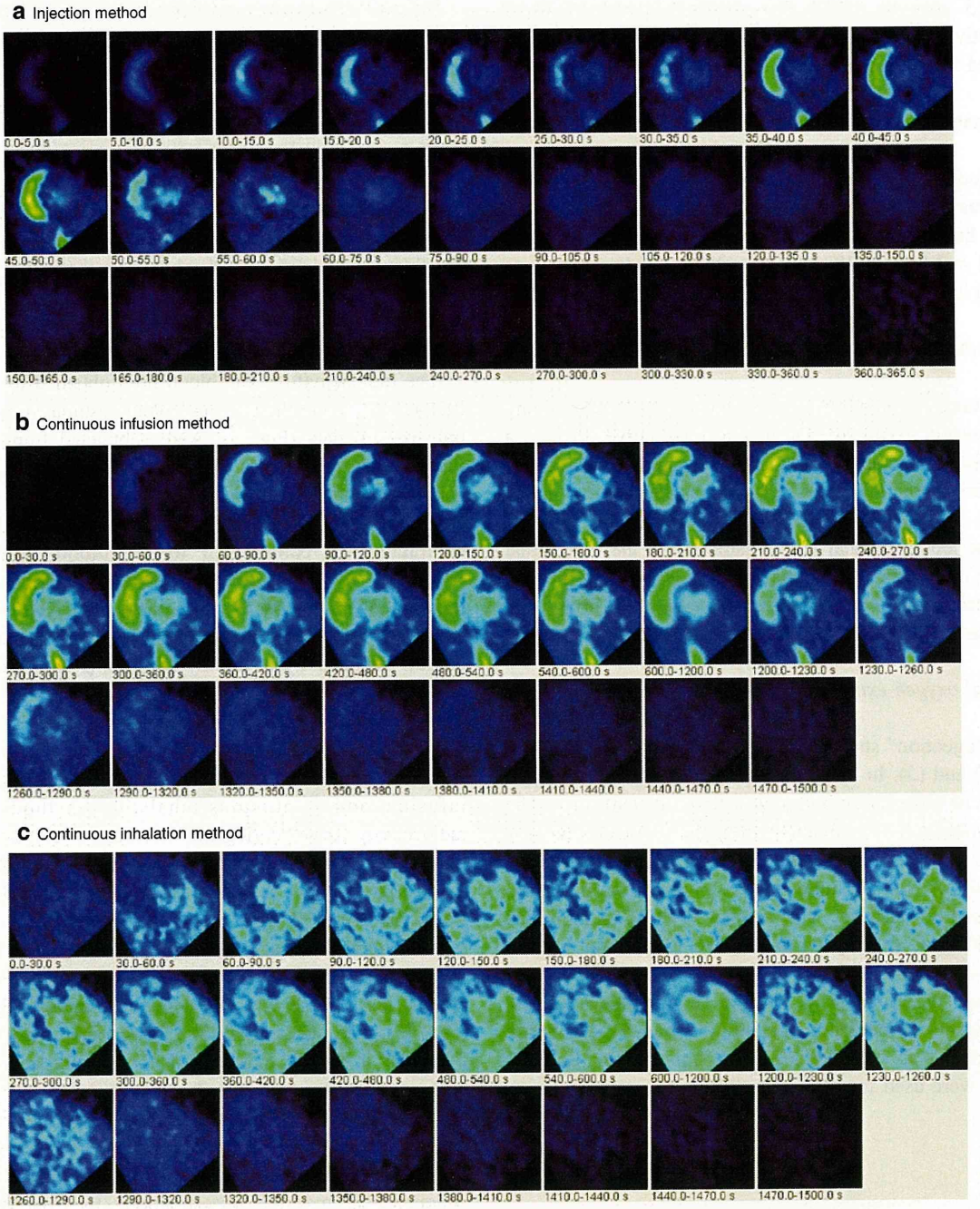

Fig. 2 PET images obtained in (**a**) the injection method, (**b**) the continuous-infusion method with injectable ^{15}O-O_2, and (**c**) the continuous-inhalation method with ^{15}O-O_2 gas

(Fig. 4b). The heart-to-lung radioactivity ratios were calculated from Fig. 4 for the quantitative estimation of image quality; the continuous-infusion method provided a ratio of 1.38±0.24, whereas the ratio was less than one with the continuous-inhalation method.

Table 2 shows the quantitative OEF values in the lateral wall obtained by the injection, continuous-infusion, and continuous-inhalation methods. These OEF values were consistent among the three methods.

Figure 5 represents the noise equivalent counts (NEC) standardized by the total counts detected by the PET scanner. Although the injection method tended to show rather high values, there was no significant difference between the values obtained by the injection and

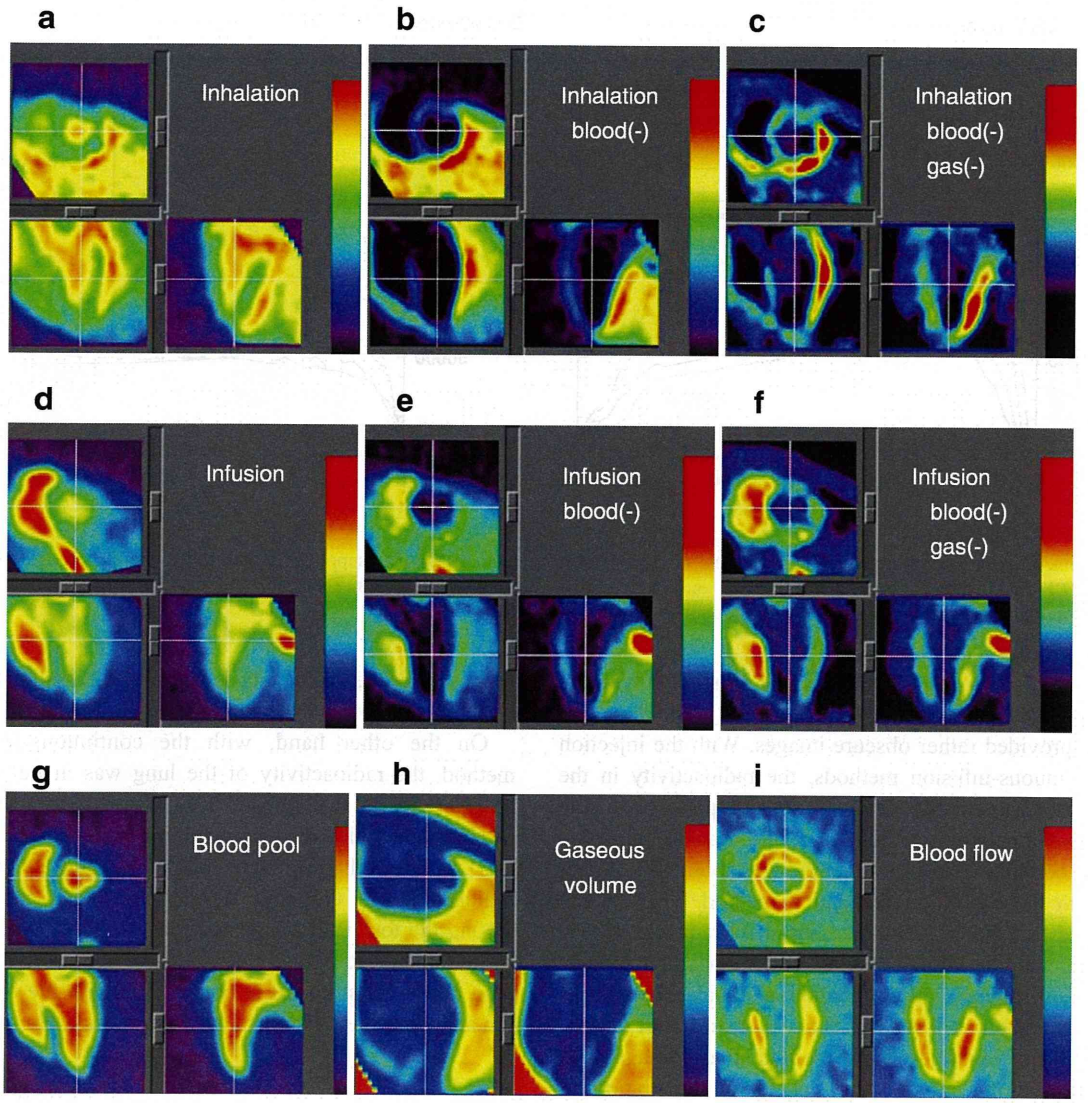

Fig. 3 PET images obtained in the study are shown. The 16th frame (steady-state frames) of the continuous-inhalation method and the continuous-infusion method are shown in (**a**) and (**d**), respectively. The 'blood-subtracted' images shown in (**b**) and (**e**) were created by subtraction of the blood-pool image by ^{15}O-CO (**g**) from (**a**) and (**d**). The 'blood- and gas-subtracted' images shown in (**c**) and (**f**) were created by the successive subtraction of the gaseous image (**h**) from (**b**) and (**e**). The myocardial blood flow image is also shown in (**i**)

continuous-infusion methods as determined by a Mann Whitney *U*-test.

Discussion

In previous studies, we showed the usefulness of the injectable ^{15}O-O_2 system for estimating cerebral oxygen metabolism in small animals such as rats under normal or ischemic conditions [10–12]. Injectable ^{15}O-O_2 replaced the inhalation protocol and radioactive ^{15}O-O_2 was administered via the tail vein. Thus, injectable ^{15}O-O_2 could abolish the artifact from the high radioactivity in the inhalation tube that distorts the PET images, especially in small animals. We considered that the concept could also be utilized in the hearts of large animals. Therefore, in the present study, we tested the feasibility of an injectable ^{15}O-O_2 system for estimating myocardial oxygen metabolism in normal pigs. In addition, since a shunt between the femoral artery and vein can be created in pigs but not in small animals, continuous infusion via the femoral shunt was also performed to achieve a constant and reliable delivery of radioactivity to the heart.

Dynamic PET scans showed a large difference in the radioactivity distribution among the three methods. Since the labeling efficiency to prepare injectable ^{15}O-O_2 was

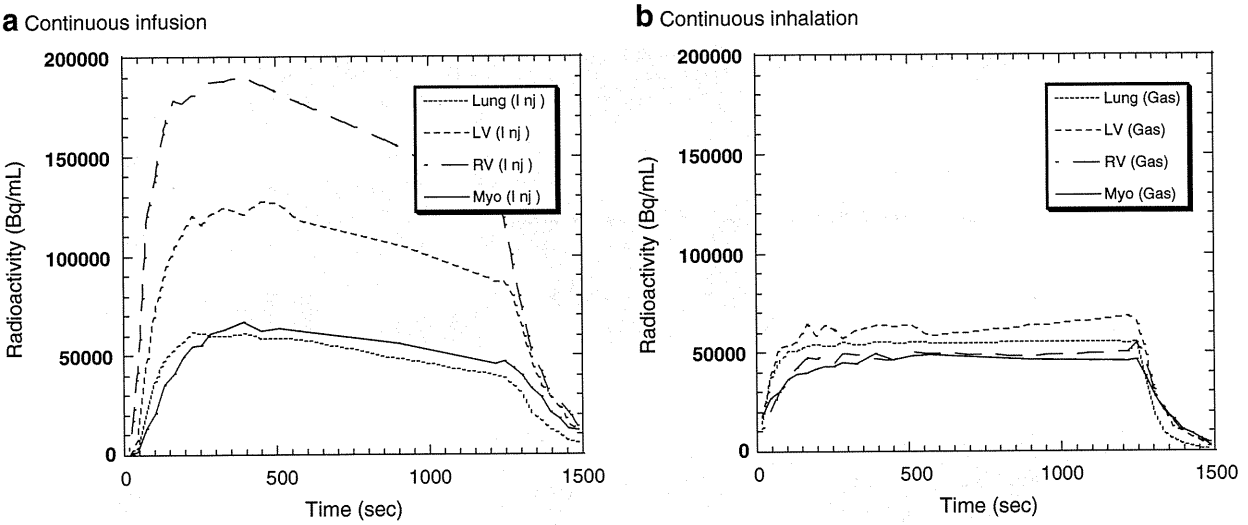

Fig. 4 Time-activity curves from the left ventricle (*LV*), the right ventricle (*RV*), the myocardium (lateral wall, Myo) and a lung region with the continuous-infusion method (**a**) and the continuous-inhalation method (**b**). The supply of radioactivity was started at time 0 s and stopped at 1,200 s. The 16th frame for the steady-state analysis was 600–1,200 s

lower with pig blood (ca. 61 MBq/ml at most) than with the blood of rats and humans (130 MBq/ml), the injection method provided rather obscure images. With the injection and continuous-infusion methods, the radioactivity in the lung was dramatically reduced in comparison to the continuous-inhalation method, since the heart-to-lung ratio with the continuous-infusion method was about 40% higher than with the continuous-inhalation method. This finding suggested that the two methods that inject radioactivity via a vein are more useful for analyzing myocardial oxygen metabolism in pigs than the continuous-inhalation method. However, a distinct difference between radioactivity of the right and left ventricles was observed in the images and time-radioactivity curves after venous administration of ^{15}O-O_2, indicating a certain degree of excretion of the radioactivity by the lung. Therefore, the spillover from the pulmonary alveoli to the myocardium could not be omitted in the two methods with venous administration, and Eq. (4) was used for the OEF analysis, although the radioactivity in the lung was lower than that in the myocardium.

On the other hand, with the continuous-inhalation method, the radioactivity of the lung was in between the radioactivity in the RV and LV. This is curious because O-15 radioactivity was supplied from the inhalation tube and transferred from the lung to blood so that the radioactivity in the lung should have been the highest among the four ROIs. This may have been caused, in part, by inhomogeneous distribution of the radioactivity in the lung due to its structure in comparison with the myocardium and ventricles, and/or by artifacts from the lung to other

Table 2 OEF estimated by the three methods using injectable ^{15}O-O_2 or ^{15}O-O_2 gas

	OEF		
	Injection	Infusion	Inhalation
Pig. 1	0.70	0.72	
Pig. 2	0.67	0.72	
Pig. 3	0.71	0.74	
Pig. 4	0.76	0.69	0.72
Average	0.71	0.72	0.72
SD	0.036	0.020	

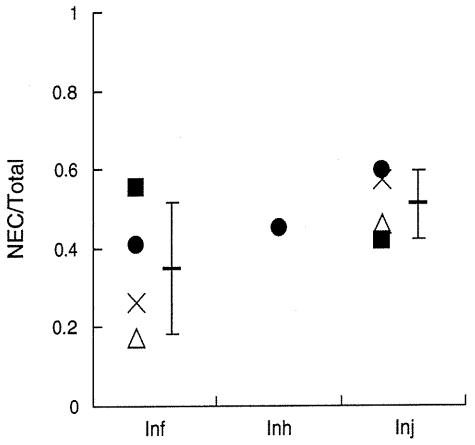

Fig. 5 The ratio of noise equivalent counts (*NEC*) to total counts in the total field of view of the PET scanner obtained with the continuous-infusion method (*Inf*), the continuous-inhalation method (*Inh*) and the injection method (*Inj*)

tissues. In any case, it is notable that the radioactivity in the myocardium was the lowest with the continuous-inhalation method, leading to difficulty in analyzing myocardial oxygen metabolism.

The OEF values in lateral walls were calculated to compare the ability of the three methods to determine myocardial oxygen metabolism by using the blood flow derived from the dual-administration protocol with the injection method and the single-administration protocol with the two continuous methods. There was no difference in the blood flow between the two protocols. Consequently, the three methods provided the same OEF value of about 0.7 and this is a physiological value in normal pigs, as was previously demonstrated [17, 18]. We have demonstrated the potential of the injectable ^{15}O-O_2 system for the estimation of physiological cerebral oxygen metabolism in rats and monkeys during early and late ischemia, hypertension, and ischemia plus hypertension [10–12, 19]. Therefore, we believe that the injection and continuous-infusion methods provide a physiological OEF in the myocardium. Nevertheless, we recognize the necessity to evaluate the reliability and usefulness of the injectable ^{15}O-O_2 method in myocardial applications. Further studies using pathophysiological animal models are required in the future, such as myocardial ischemia, hypoxia, and heart failure. On the other hand, since $MMRO_2$ is basically regarded as the product of MBF and OEF, the results indicated that these three methods were equivalent in their ability to quantify $MMRO_2$ in normal pigs, at least in the lateral wall. Although the images after the subtraction of spillovers from blood and gas showed different contrast between the continuous-infusion and continuous-inhalation methods, the ability of these two methods to measure OEF and $MMRO_2$ in the lateral walls was equivalent.

We did not evaluate myocardial oxygen metabolism in other heart regions since the radioactivity in the right ventricle could not be removed due to a significant difference of radioactivity between the ventricles with the continuous-infusion method. The injection method might be able to evaluate oxygen metabolism in other regions besides the lateral wall, although this was not evaluated in this study due to the low radioactivity of injectable ^{15}O-O_2 as described above. In the injection method, O-15 radioactivity was delivered from the femoral vein to RV, the lung, LV, and finally the myocardium. Thus, when the LV and myocardial activity reach a maximum, the RV activity is expected to be low. The later frames of the dynamic PET images with the injection method might avoid the high RV activity and delineate the myocardium and LV more clearly. With accurate anatomical information by gated PET/CT, the injection method will provide oxygen metabolism in other heart regions. In addition, the injection method has a benefit in that it is noninvasive and shortens the acquisition time in comparison with the continuous-infusion method. Future studies are needed to determine whether the injectable ^{15}O-O_2 system can be used in other heart regions.

With the injection method, the ratio of noise equivalent counts (NEC) to total counts tended to be the higher, probably because of the absence of high radioactivity adjacent to the PET scanner. Nevertheless, the continuous-infusion method did not show this tendency. This may be because tubes for the input to the artificial lung were positioned at the femoral shunt and the output to the drain of O-15 gas was positioned alongside the PET scanner, resulting in an increase of random counts during the study. Also, it is notable that the value with the continuous-inhalation method was not small, which suggests that the inhalation protocol itself did not worsen the results, but rather the high radioactivity in the lung might affect the analysis. In any case, if more care is given to shielding of the radioactivity in tubes and/or for arrangement of instruments in the PET room, a higher value of NEC/total counts will be obtained with the injectable ^{15}O-O_2 system.

The declining slope delineated in the time-activity curves with the continuous-infusion method requires some explanation. Since the flow rate of O-15 gas supply to the artificial lung positioned at the femoral shunt was maintained constant during the PET scan, it is possible that a decrease of labeling efficiency of the artificial lung occurred due to the deposition of any components of blood. The blood of rats or humans was negligibly deposited in the artificial lung during circulation at the same rate for at least 30 min in our other experiments, so that this problem may be specific for pigs. It is unclear which component in pig blood was exactly involved in the deposition and three of four pigs did not show a declining slope of the time-activity curve.

In practice, in routine studies on myocardial oxygen metabolism using large animals such as pigs, the continuous-inhalation method with ^{15}O-O_2 gas may be easier to perform for the following reasons: (1) the intubation tube used for gas anesthesia prior to the PET scan can also be used for ^{15}O-O_2 gas inhalation; (2) catheterization of the femoral artery and vein to create the femoral shunt for the continuous-infusion method may be troublesome; and (3) the injection of ^{15}O-O_2 requires an artificial lung, preparation time, and blood taken from the same animal prior to the PET scan. However, the injection of ^{15}O-O_2 has a substantial advantage over the continuous-inhalation method in that there is reduced radioactivity in the lung and clearer images of the heart are obtained. Therefore, the method for estimating myocardial oxygen metabolism should be selected depending on the objectives of the study and the surgical procedures. Furthermore, since radioactivity administered into the femoral vein is partially excreted into expired air, the injectable ^{15}O-O_2 system might be used for evaluating pulmonary function in the future.

Conclusion

In this study, we tested the feasibility of using an injectable ^{15}O-O_2 system to estimate myocardial oxygen metabolism in pigs. Both the bolus-injection and continuous-infusion methods reduced the radioactivity in the lung and provided similar OEF values in the lateral walls of the heart. These findings indicate that the injectable ^{15}O-O_2 system has the potential to evaluate myocardial oxygen metabolism.

References

1. Ohtake T. The review of myocardial positron emission computed tomography and positron imaging by gamma camera. Kaku Igaku. 1998;35:179–87.
2. Klein LJ, Visser FC, Knaapen P, Peters JH, Teule GJ, Visser CA, et al. Carbon-11 acetate as a tracer of myocardial oxygen consumption. Eur J Nucl Med. 2001;28:651–68.
3. Schelbert HR. PET contributions to understanding normal and abnormal cardiac perfusion and metabolism. Ann Biomed Eng. 2000;28:922–9.
4. Visser FC. Imaging of cardiac metabolism using radiolabelled glucose, fatty acids and acetate. Coron Artery Dis. 2001;12(Suppl 1):S12–8.
5. Hata T, Nohara R, Fujita M, Hosokawa R, Lee L, Kudo T, et al. Noninvasive assessment of myocardial viability by positron emission tomography with ^{11}C acetate in patients with old myocardial infarction. Usefulness of low-dose dobutamine infusion. Circulation. 1996;94:1834–41.
6. Yamamoto Y, de Silva R, Rhodes CG, Iida H, Lammertsma AA, Jones T, et al. Noninvasive quantification of regional myocardial metabolic rate of oxygen by $^{15}O_2$ inhalation and positron emission tomography. Experimental validation. Circulation. 1996;94:808–16.
7. Iida H, Rhodes CG, Araujo LI, Yamamoto Y, de Silva R, Maseri A, et al. Noninvasive quantification of regional myocardial metabolic rate for oxygen by use of $^{15}O_2$ inhalation and positron emission tomography. Theory, error analysis, and application in humans. Circulation. 1996;94:792–807.
8. Shidahara M, Watabe H, Kim KM, Oka H, Sago M, Hayashi T, et al. Evaluation of a commercial PET tomograph-based system for the quantitative assessment of rCBF, rOEF and $rCMRO_2$ by using sequential administration of ^{15}O-labeled compounds. Ann Nucl Med. 2002;16:317–27.
9. Mintun MA, Raichle ME, Martin WR, Herscovitch P. Brain oxygen utilization measured with O-15 radiotracers and positron emission tomography. J Nucl Med. 1984;25:177–87.
10. Magata Y, Temma T, Iida H, Ogawa M, Mukai T, Iida Y, et al. Development of injectable O-15 oxygen and estimation of rat OEF. J Cereb Blood Flow Metab. 2003;23:671–6.
11. Temma T, Magata Y, Kuge Y, Shimonaka S, Sano K, Katada Y, et al. Estimation of oxygen metabolism in a rat model of permanent ischemia using positron emission tomography with injectable ^{15}O-O_2. J Cereb Blood Flow Metab. 2006;26:1577–83.
12. Temma T, Kuge Y, Sano K, Kamihashi J, Obokata N, Kawashima H, et al. PET O-15 cerebral blood flow and metabolism after acute stroke in spontaneously hypertensive rats. Brain Res. 2008;1212:18–24.
13. Watabe H, Jino H, Kawachi N, Teramoto N, Hayashi T, Ohta Y, et al. Parametric imaging of myocardial blood flow with ^{15}O-water and PET using the basis function method. J Nucl Med. 2005;46:1219–24.
14. Iida H, Rhodes CG, de Silva R, Yamamoto Y, Araujo LI, Maseri A, et al. Myocardial tissue fraction–correction for partial volume effects and measure of tissue viability. J Nucl Med. 1991;32:2169–75.
15. Wienhard K, Dahlbom M, Eriksson L, Michel C, Bruckbauer T, Pietrzyk U, et al. The ECAT EXACT HR: performance of a new high resolution positron scanner. J Comput Assist Tomogr. 1994;18:110–8.
16. Kudomi N, Hayashi T, Teramoto N, Watabe H, Kawachi N, Ohta Y, et al. Rapid quantitative measurement of $CMRO_2$ and CBF by dual administration of ^{15}O-labeled oxygen and water during a single PET scan-a validation study and error analysis in anesthetized monkeys. J Cereb Blood Flow Metab. 2005;25:1209–24.
17. Alders DJ, Groeneveld AB, de Kanter FJ, van Beek JH. Myocardial O_2 consumption in porcine left ventricle is heterogeneously distributed in parallel to heterogeneous O_2 delivery. Am J Physiol Heart Circ Physiol. 2004;287:H1353–61.
18. Van Woerkens EC, Trouwborst A, Duncker DJ, Koning MM, Boomsma F, Verdouw PD. Catecholamines and regional hemodynamics during isovolemic hemodilution in anesthetized pigs. J Appl Physiol. 1992;72:760–9.
19. Temma T, Magata Y, Iida H, Hayashi T, Ogawa M, Mukai T, et al. Development of injectable O-15 oxygen and its application for estimation of OEF. International Congress Series, Quantitation in Biomedical Imaging with PET and MRI Proceedings of the International Workshop on Quantitation in Biomedical Imaging with PET and MRI. 2004;1265:262–65.

J Fluoresc (2010) 20:225–234
DOI 10.1007/s10895-009-0542-3

ORIGINAL PAPER

Synthesis of a New NIR Fluorescent Nd Complex Labeling Agent

Kazuki Aita · Takashi Temma · Yoichi Shimizu · Yuji Kuge · Koh-ichi Seki · Hideo Saji

Received: 15 June 2009 / Accepted: 15 September 2009 / Published online: 10 October 2009

Abstract Fluorescent analysis has been widely used in biological, chemical and analytical research. A useful fluorescent labeling agent should include NIR emission, a large Stoke's shift, and good labeling ability without interfering with the pharmacological profile of the labeled compound. Thus, we planned to develop an M-AMF-DOTA(Nd) derivative composed of an NIR fluorescent moiety and a maleimide conjugating moiety as a new NIR fluorescent labeling agent which fulfills these requirements. M-AMF-DOTA(Nd) was synthesized from 4-amino-fluorescein and was conjugated with an avidin molecule (Avidin-AMF-DOTA(Nd)) through Lys-side chains by reaction with 2-iminothiolane. The fluorescent features of M-AMF-DOTA(Nd) and Avidin-AMF-DOTA(Nd) were comparatively evaluated. A binding assay of Avidin-AMF-DOTA(Nd) with D-biotin and a tumor cell-uptake study were performed to estimate the effects of conjugation on the biological and physicochemical features of the protein. M-AMF-DOTA(Nd) was obtained in 22% overall yield. M-AMF-DOTA(Nd) had a typical NIR fluorescence from the Nd ion (880 nm and 900 nm from 488 nm excitation). Avidin-AMF-DOTA(Nd) was easily synthesized and also had typical NIR fluorescence from the Nd ion without loss of fluorescent intensity. The binding affinity of Avidin-AMF-DOTA(Nd) to D-biotin was equivalent to naive avidin. Avidin-AMF-DOTA(Nd) was taken up by tumor cells in the same manner as avidin conjugated with fluorescein isothiocyanate, an established, widely used fluorescent avidin. Results from this study indicate that M-AMF-DOTA(Nd) is a potential labeling agent for routine NIR fluorescent analysis.

Keywords Neodymium · Near-infrared · Fluorescent labeling · Maleimide

K. Aita · T. Temma · Y. Shimizu · Y. Kuge · H. Saji (✉)
Department of Patho-Functional Bioanalysis,
Graduate School of Pharmaceutical Sciences, Kyoto University,
Kyoto, Japan
e-mail: hsaji@pharm.kyoto-u.ac.jp

K. Aita · K. Seki
Central Institute of Isotope Science, Hokkaido University,
Sapporo, Hokkaido, Japan

Y. Kuge
Department of Tracer Kinetics & Bioanalysis,
Graduate School of Medicine, Hokkaido University,
Sapporo, Hokkaido, Japan

Introduction

Fluorescent imaging, one of several molecular imaging techniques, is a very convenient method because of its simple and safe operation, high spatial resolution, and short detection time. Fluorescent labels are widely used for applications in biology [1], biotechnology [2], medicine [3], and in combinatorial chemistry [4] as encoders of individual library members and as reporters of chemical reactions. Fluorescent labeling agents should not influence the pharmacological character of a labeled compound. In addition, near-infrared (NIR) fluorescence and a large Stoke's shift are desirable characteristics of labeling agents in the fields of biology, biotechnology, and medicine since NIR light has good permeability in living organisms and there is negligible self-fluorescence in the NIR region. A large Stoke's shift makes it easier to remove scattered and reflected excitation light by suitable optical filters. However, there are few agents that possess all of these features. Thus, we planned to develop a novel

fluorescent labeling agent for fluorescent imaging of proteins in living organisms.

We recently reported new NIR fluorescent dyes with low molecular weight, 4AMF-DOTA(Nd) (MW=883) [5] and PAN-DOTA(Yb) (MW=823) [6], which include lanthanide complexes in their structures. They had NIR emission and large Stoke's shifts (880 and 900 nm from 488 nm excitation light for 4AMF-DOTA(Nd), 975 nm from 530 nm excitation light for PAN-DOTA(Yb)). Their emission wavelengths were constant under various conditions (pH and solvents). Therefore, these NIR fluorescent dyes are promising candidates for use as fluorescent labeling agents with some modification. In this regard, we selected 4AMF-DOTA(Nd) as the starting structure of the labeling agent because it has several functional groups capable of being modified to bind with a functional molecule and at the excitation wavelength it has a stronger absorption and gives a more potent signal intensity than PAN-DOTA(Yb).

A conjugating moiety was required to link 4AMF-DOTA (Nd) and a functional molecule. As a conjugating moiety, maleimide was selected because it has very fast reactivity, good selectivity, and makes a very stable bond with thiols. Maleimide was linked to one of the DOTA carboxyl groups [7], and the remaining carboxyl groups were capped as amides in order to avoid changes in fluorescence and chelating ability since carboxyl groups often interact with cationic groups and solutes which might alter the fluorescence properties of the complex. The selection of a suitable spacer between the fluorophore and the conjugation moiety is also important. We selected a 6-atom ethyl-propyl amide chain as the spacer because moderately inflexible chains composed of 6~12 atoms have been adopted as an appropriate length and rigidity to suppress interaction between the labeled molecule and the fluorophore, which otherwise could result in altered fluorescence as well as chemical and physical properties of the labeled molecule [8–12].

The above analysis led to the design and synthesis of M-AMF-DOTA(Nd) that includes a maleimide (Scheme 1) as a new NIR fluorescent labeling agent with a large Stoke's shift. In addition, we have evaluated the imaging potential of M-AMF-DOTA(Nd) conjugated to avidin (Avidin-AMF-DOTA(Nd)) through binding experiments with biotin and in tumor cell-uptake studies.

Materials and methods

Materials

All chemicals used in this study were commercial products of the highest purity and if necessary were further purified by standard methods. Avidin and D-biotin were purchased from Nacalai Tesque, Inc. (Kyoto, Japan). ^{125}I-iodide was purchased from Perkin Elmer Life and Analytical Sciences (Boston, MA). C6 glioma cells were purchased from the Health Science Research Resources Bank (Tokyo, Japan).

Instruments

FT-IR spectra were recorded with a Shimadzu, IRAffinity-1 (Shimadzu Corporation, Kyoto, Japan). UV-vis spectra were measured using a UV-1800 (Shimadzu Corporation, Kyoto, Japan). ESI-MS measurements were performed on a Shimadzu LC-MS2010 EV (Shimadzu Corporation, Kyoto, Japan). ^{1}H-NMR spectra were recorded on a JEOL JNM-AL400 (JEOL Ltd., Tokyo, Japan). Fluorescent spectroscopy was performed with a Fluorolog-3 with a NIR sensitive photomultiplier detection system (~1200 nm) (HORIBA Jobin Yvon Inc., Kyoto, Japan). The slit width was 10 nm for both excitation and emission measurements. Time-resolved fluorescence spectra were recorded on a Fluorolog-3 with Phosphorescence (HORIBA Jobin Yvon Inc., Kyoto, Japan). The slit width was 12 nm for both excitation and emission. In both fluorescence spectra measurements, the photomultiplier voltage was 1450 V. Flow cytometry was performed on a FACScan (Becton Dickinson Inc., Franklin Lakes, NJ, USA). Radioactivities were counted by Cobra Auto-Gamma Counter 5010 (Packard instruments Co., Downers Grove, IL, USA). Fluorescent images were photographed with a ChemiDoc XRS (Bio-Rad Japan, Tokyo, Japan).

Fluorescence emission and excitation spectral measurements

The fluorescence emission spectra of M-AMF-DOTA(Nd), M-AMF-DOTA, Avidin-AMF-DOTA(Nd), and 4AMF-DOTA(Nd) (10 μM) were measured in 10 mM Tris-HCl buffer (pH 8.0) at 25 °C, following excitation at 488 nm.

UV-visible absorption spectral measurements

The absorption spectral changes of AMF-DOTA(Nd), M-AMF-DOTA and M-AMF-DOTA(Nd) (10 μM) in 10 mM Tris-HCl buffer (pH 8.0) at 25 °C were determined.

Quantum yield analysis

Quantum yield analyses of M-AMF-DOTA(Nd) and 4AMF-DOTA(Nd) were measured by a previously reported method [13] in 10 mM Tris-HCl buffer (pH 8.0) at 25 °C, following excitation at 488 nm and emission at 880 nm. The reference compound, [Yb(Tropolonate)$_4$], was measured at 380 nm excitation and 975 nm emission in 10 mM

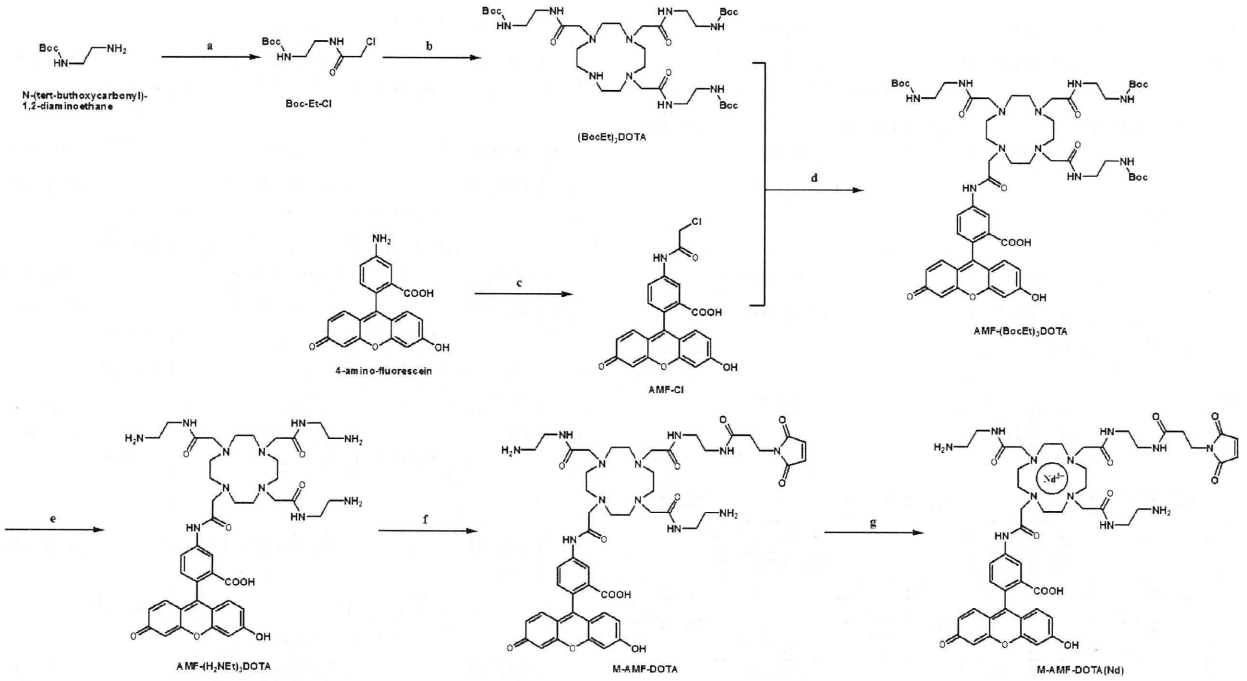

Scheme 1 Synthetic scheme of M-AMF-DOTA(Nd). Reagents and conditions: **a**) chloroacetyl chloride, 0 °C, 3 h, **b**) cyclen 4HCl, $^{i}Pr_2EtN$, 80 °C, 9 h, **c**) chloroacetyl chloride, 0 °C, 1 h, **d**) K_2CO_3, 80 °C, 7 h, **e**) TFA, 0 °C, 10 min, **f**) N-succinimidyl-3-maleimidepropionate, Et_3N, room temperature, 1 h, **g**) $NdCl_3$ $6H_2O$

Tris-HCl buffer. The absorbance of the samples was adjusted to not exceed 0.2 at the excitation wavelength. The wavelength dependence on excitation light intensity and the detection efficiency of emission light were as given from HORIBA Jobin Yvon Inc.

Time-delayed fluorescence spectral measurement

The time-delayed fluorescence spectra of M-AMF-DOTA(Nd) (10 μM) were measured in 10 mM Tris-HCl buffer (pH 8.0) at 25 °C, following excitation at 488 nm. A delay time of 7 μs and a gate time of 100 μs were used.

Fluorescence lifetime measurements

The fluorescence lifetime of M-AMF-DOTA(Nd) (10 μM) in 10 mM Tris-HCl buffer (pH 8.0) at 25 °C was determined. The data, obtained by monitoring the emission intensity at 880 nm (λ_{ex}=488 nm), were collected at a resolution of 1 μs and were fit to a single-exponential curve using the equation shown below (Eq. 1), where I_0 and I are the fluorescence intensities at time t=0 and time t, respectively, and τ is the fluorescence emission lifetime.

$$I = I_0 \exp(-t/\tau) \quad (1)$$

Biotin competitive assay

[^{125}I]-IBB ([^{125}I]-(3-iodobenzoyl)norbiotinamide) was prepared as previously described [14]. [^{125}I]-IBB (0.5 mCi/mL) 10 μL, D-biotin (5, 50, 500, 1000 mM) 100 μL, and PBS 290 μL were added to a microtube containing 100 μL of Avidin-AMF-DOTA(Nd) (80 μg/mL) or avidin (80 μg/mL). The reaction was performed at 37 °C for 1 h. The reaction mixture was applied to an Amicon Microcon filter (Millipore) and centrifuged at 4 °C, 1467 × g for 30 min (Micro Cooling Centrifuge 1720, Kubota, Osaka, Japan). The radioactivities of the reactant and filtrate were then measured, and the binding rate was calculated.

Cellular uptake study of Avidin-AMF-DOTA(Nd) and Avidin-FITC

C6 glioma cells were maintained at 37 °C in a humidified atmosphere containing 5% CO_2 in Dulbecco's modified eagle medium (DMEM) and 10% fetal bovine serum. Avidin-AMF-DOTA(Nd) or avidin conjugated to fluorescein isothiocyanate (Avidin-FITC) (50 μg/mL in DMEM, 1.0 mL) were added to C6 glioma cells (1×10^5 cells/dish) and incubated for 1, 3, or 6 h. After incubation, the cells were twice washed with PBS(-), and then treated with trypsin to release them from the dish. Fluorescence levels were

measured using a flow cytometer. Fluorescence intensities were normalized for quantum yield (φ=0.21 and 0.60 for Avidin-AMF-DOTA(Nd) and Avidin-FITC, respectively) and the number of labeling agents (2.5 and 4.0 for Avidin-AMF-DOTA(Nd) and Avidin-FITC, respectively).

Synthesis

4-(Chloromethylamide)fluorescein (4AMF-Cl) [5] and radiolabeled IBB ([^{125}I]-IBB) [14] were prepared as previously described.

N-tert-buthoxycarbonyl-2-(2-chloroacetoamide)-aminoethane (Boc-Et-Cl)

To a $CHCl_3$ solution (100 mL) of N-(tert-buthoxycarbonyl)-1,2-diaminoethane (1.60 g, 10 mmol) and Et_3N (10.1 g, 100 mmol) was slowly added $ClCH_2COCl$ (1.13 g, 10 mmol) in $CHCl_3$ solution (20 mL) at 0 °C. The solution was stirred for 3 h and then evaporated to remove the solvent. The black-yellow residue was purified by silica gel column chromatography to obtain Boc-Et-Cl as a pale yellow powder (2.0 g, 8.5 mmol, 85%)

LR-MS(ESI, neg.) m/z found 237 ([M+H]$^+$), calcd. 237
HR-MS (FAB, pos.) m/z found 237.0928, calcd. 237.0928 ($C_9H_{18}ClN_2O_3$)
^{1}H-NMR (400 MHz, $CDCl_3$) δ 4.83 (2H, s), 3.46 (2H, t, J=7.3 Hz), 3.25 (2H, t, J=7.3 Hz), 1.45 (9H, s)

1,4,7-tris(2-(tert-butoxycarbonyl)-2-amino-ethylamidemethyl)- 1,4,7,10-tetraazacyclododecane ((BocEt)$_3$DOTA)

To a dry MeCN solution (50 mL) of 1,4,7,10-tetraazacyclododecane tetrahydrochloride (cyclen 4HCl) (318 mg, 1.0 mmol), ^{i}Pr$_2$EtN (1.3 g, 10.0 mmol) was added, and the reaction was stirred for 5 min at 40 °C under anaerobic conditions. Then Boc-Et-Cl (708 mg, 3 mmol) in dry MeCN solution (10 mL) was slowly added to the suspension. After stirring for 9 h at 80 °C, the solution was evaporated to remove the solvent. The pale yellow residue was purified by silica gel column chromatography to obtain (BocEt)$_3$DOTA as a white powder (320 mg, 0.4 mmol, 41%)

LR-MS(ESI, neg.) m/z found 774 ([M+H]$^+$), calcd. 774
HR-MS (FAB, pos.) m/z found 773.5171 calcd. 773.5171 ($C_{32}H_{62}N_{10}O_9$)
^{1}H-NMR (400 MHz, CD_3OD) δ 3.52–2.64 (34H, m), 1.50 (27H, s)

1-(4-Amidemethyl-fluorescein)-4,7,10-tris (2-(tert-butoxycarbonyl)-2-amino-ethylamidemethyl)-1,4,7, 10-tetraazacyclododecane (AMF-(BocEt)$_3$DOTA)

A dry DMF solution (10 mL) of (BocEt)$_3$DOTA (150 mg, 0.2 mmol) and K_2CO_3 (0.7 g, 5.0 mmol) was stirred for 5 min at 80 °C under anaerobic conditions. To the solution was slowly added 4-AMF-Cl (85 mg, 0.2 mmol) in dry DMF solution (10 mL). After stirring for 7 h at 80 °C, the solution was evaporated to remove the solvent. The resulting residue was redissolved in a minimum amount of MeOH, the solution was poured into Et_2O (20 mL), and the resulting residue was washed three times with Et_2O by decantation. The powder was dried under vacuum to obtain AMF-(BocEt)$_3$DOTA (139 mg, 0.14 mmol, 60%) as a red powder.

LR-MS(ESI, pos.) m/z found 1161 ([M+H]$^+$), calcd. 1161
HR-MS (FAB, pos.) m/z found 1160.5914 calcd. 1151.5914 ($C_{57}H_{82}N_{11}O_{15}$)
^{1}H-NMR (400 MHz, CD_3OD) δ 8.38 (1H, s), 7.91 (1H, d, J=7.3 Hz), 6.62 (3H, m), 6.52 (2H, s), 6.44 (2H, dd, J=1.9, 8.7 Hz), 3.51–2.66 (36H, m), 1.42 (27H, s)

1-(4-Amidemethyl-fluorescein)-4,7,10-tris (2-amino-ethylamidemethyl)-1,4,7, 10-tetraazacyclododecane (AMF-(H$_2$NEt)$_3$DOTA)

TFA (2.0 mL) was slowly added to a MeOH solution of AMF-(BocEt)$_3$DOTA (116 mg, 0.1 mmol) at 0 °C. The solution was stirred for 10 min, and the mixture was evaporated to remove the solvent. The resulting residue was redissolved in a minimum amount of MeOH and evaporated. This procedure was repeated three times. The resulting powder was dried under vacuum to obtain AMF-(H$_2$NEt)$_3$DOTA (85 mg, 0.1 mmol, 99%) as an orange powder.

LR-MS(ESI, pos.) m/z found 860 ([M+H]$^+$), calcd. 860
HR-MS (FAB, pos.) m/z found 860.4341 calcd. 860.4341 ($C_{42}H_{58}N_{11}O_9$)
^{1}H-NMR (400 MHz, CD_3OD) δ 8.38 (1H, s), 7.91 (1H, d, J=7.3 Hz), 6.62 (3H, m), 6.52 (2H, s), 6.44 (2H, dd, J=1.9, 8.7 Hz), 3.53-2.62 (36H, m)

1-(4-Amidemethyl-fluorescein)-4,10-di(2-amino-ethylamidemethyl)-7-(2-(3-maleimidopropionate)-2-amino-ethylamidemethyl)-1,4,7,10-tetraazacyclododecane (M-AMF-DOTA)

To a dry DMF solution (10 mL) of AMF-(H$_2$NEt)$_3$DOTA (85 mg, 0.1 mmol) and Et_3N (100 mg, 1.0 mmol) was added N-succinimidyl-3-maleimidepropionate (26 mg,

0.1 mmol), and the reaction was stirred for 1 h at room temperature under anaerobic conditions. The solution was evaporated to remove the solvent. The resulting residue was redissolved in a minimum amount of MeOH. The solution was poured in Et_2O (5 mL), and the resulting residue was washed three times with Et_2O by decantation. The powder was dried under vacuum to obtain M-AMF-DOTA (55 mg, 0.05 mmol, 55%) as a red powder.

LR-MS(ESI, neg.) m/z found 504 ($[M-2H]^{2-}$), calcd. 504
HR-MS (FAB, neg.) m/z found 1009.4610 calcd. 1009.4610 ($C_{49}H_{61}N_{12}O_{12}$)
^{1}H-NMR (400 MHz, CD_3OD) δ 8.38 (1H, s), 7.91 (1H, d, J=7.3 Hz), 6.62 (3H, m), 6.52 (2H, s), 6.92 (2H, d, J=7.3 Hz), 6.44 (2H, dd, J=1.9, 8.7 Hz), 3.51–2.43 (40H, m)

M-AMF-DOTA(Nd)

To an EtOH solution (10 mL) of M-AMF-DOTA (10.1 mg, 10 μmol) was added $NdCl_3$ $6H_2O$ (3.6 mg, 10 μmol). After stirring for 1 h at room temperature in the dark, the reaction mixture was filtered. The filtrate was evaporated and dried in vacuo to obtain M-AMF-DOTA(Nd) (10.4 mg, 9.0 μmol, 90%) as a red powder.

LR-MS (ESI, pos.) m/z found 576 ($[M-H]^{2+}$), calcd. 576
HR-MS (FAB, pos.) m/z found 1150.3531 calcd. 1150.3531 ($C_{49}H_{60}N_{12}NdO_{12}$)

Avidin-AMF-DOTA(Nd)

To avidin (1.0 mg, 15 nmol) in borate buffer (0.16 M with 2 mM EDTA, 100 μL) was added 2-iminothiolane (255 μg, 185 nmol) in borate buffer (0.16 M with 2 mM EDTA, 25.5 μL). After incubation at room temperature for 1 h, dithiothreitol (30.8 μg, 2.0 μmol) in H_2O (2.0 μL) was added to the reaction mixture, and the reaction was allowed to stand for 15 min. After purification of the thiolated avidin by spin-column (Sephadex G50, GE healthcare UK Ltd.), a solution of PBS (0.1 M, pH 7.4, 172 μL) containing M-AMF-DOTA(Nd) (1.7 mg, 1.5 μmol) was added. The mixture was incubated at 37 °C for 1 h in the dark. After incubation, N-ethyl maleimide (40 μg, 32 nmol) in DMSO (4.0 μL) was added to cap unreacted thiols and the reaction was further incubated at room temperature for 30 min in the dark. After size-exclusion filtration twice with a PD-10 column (17-0851-01, GE Healthcare UK Ltd.) using 0.1 M PBS (pH 7.4), Avidin-AMF-DOTA(Nd) was obtained.

The fluorescence spectrum of Avidin-AMF-DOTA(Nd) was measured by Fluorolog-3. The progress of the labeling reaction was confirmed by electrophoresis. Avidin-AMF-DOTA(Nd) and Avidin-AMF-DOTA were denatured in PBS by heating at 100 °C for 5 min. Then samples (10 μL in each well) were separated by one-dimensional denaturing sodium dodecyl sulfate-polyacrylamide gel electrophoresis (SDS-PAGE) with a 5% to 20% gradient polyacrylamide gel (ePAGEL E-T520L, ATTO). A standard marker (Precision Plus Protein™ Standards, BIO-RAD) was used as a protein molecular weight marker. After electrophoresis using the AE-8155 myPower-II 500 (ATTO) at 400 V, 20 mA for 70 min, the gel was stained with Coomassie Brilliant Blue R250 (CBB) to visualize the proteins.

The number of thiols introduced per avidin was calculated by the following method: 4,4′-dithiodipyridine (22 μg in 0.1 M PBS (pH 7.4, 20 μL)) was added to thiolated avidin (85 μg in 0.1 M PBS (pH 7.4, 500 μL)), and the reaction was incubated at 30 °C for 30 min. After incubation, the absorbances of the reaction mixture at 280 nm and 324 nm were measured to calculate the number of thiols (ε=113,900, 7,060 for avidin and thiol, respectively) using the equation below (Eq. 2).

$$\text{Number of thiol} = \frac{(A_{342}/\varepsilon_{\text{thiol}})}{A_{280}/\varepsilon_{\text{avidin}}} \quad (2)$$

The number of M-AMF-DOTA(Nd) and M-AMF-DOTA per avidin were calculated by the equation below (Eq. 3) using the absorbances measured at 280 and 488 nm of Avidin-AMF-DOTA(Nd) or Avidin-AMF-DOTA (ε= 113,900, 18,000 and 18,000 L/(M*cm) for avidin, AMF-DOTA(Nd) and AMF-DOTA, respectively).

$$\text{Number of dye} = \frac{(A_{488}/\varepsilon_{\text{dye}})}{(A_{280}/\varepsilon_{\text{avidin}})} \quad (3)$$

Avidin-FITC

To avidin (1.1 μg, 17 nmol) in 20 mM Na_2HPO_4 (aq) (112 mL) was added FITC-I (126 μg, 322 nmol) in DMSO (12.6 μL). The mixture was incubated at room temperature for 1 h in the dark. After incubation, the mixture was purified by size-exclusion filtration with a PD-10 column (17-0851-01, GE Healthcare UK Ltd.) using 0.1 M PBS (pH 7.4) to obtain Avidin-FITC.

The fluorescence of Avidin-FITC was measured by Fluorolog-3. SDS-PAGE and CBB staining of Avidin-FITC were performed by the same methods as for Avidin-AMF-DOTA. The number of FITC groups introduced onto avidin was calculated by the same method as for Avidin-AMF-DOTA (ε=113,900 and 80,000 L/(M*cm) for avidin and FITC (488 nm), respectively).

Results

Synthesis and characterization of M-AMF-DOTA(Nd)

M-AMF-DOTA was synthesized from 4-amino-fluorescein and cyclen in six steps as shown in Scheme 1. The overall yield from 4-aminofluorescein was 24%. M-AMF-DOTA (Nd) was easily synthesized in 90% yield by stirring M-AMF-DOTA and $NdCl_3$ in MeOH.

In the IR spectra, amide-I absorptions were observed at 1558 cm^{-1} for M-AMF-DOTA and 1571 cm^{-1} for M-AMF-DOTA(Nd), and amide-II absorptions were found at 1635 cm^{-1} for M-AMF-DOTA and 1651 cm^{-1} for M-AMF-DOTA(Nd) (data not shown).

The UV-vis absorption spectra of M-AMF-DOTA(Nd), M-AMF-DOTA and 4AMF-DOTA(Nd) in buffer are shown in Fig. 1A. Each spectrum shows the same strong absorption peak at 490 nm.

The emission spectra of M-AMF-DOTA(Nd), M-AMF-DOTA and 4AMF-DOTA(Nd) in buffer are shown in Fig. 1B. Typical characteristic peaks at 880 nm and 900 nm were detected in the M-AMF-DOTA(Nd) and 4AMF-DOTA(Nd) spectra (λ_{ex}=488 nm). In contrast, characteristic fluorescence peaks were not detected for M-AMF-DOTA under the same conditions. The 880 nm and 900 nm emission signals for M-AMF-DOTA(Nd) were slightly stronger than for 4AMF-DOTA(Nd). The quantum yields of M-AMF-DOTA(Nd) and 4AMF-DOTA(Nd) were calculated to be 1.2×10^{-5} and 4.5×10^{-6}, respectively.

The excitation spectra of M-AMF-DOTA(Nd), M-AMF-DOTA and 4AMF-DOTA(Nd) in buffer are shown in Fig. 1C (λ_{em}=880 nm for M-AMF-DOTA(Nd) and 4AMF-DOTA(Nd) or 515 nm for M-AMF-DOTA). Each spectrum shows the same excitation peak at 490 nm.

Long-lived fluorescence measurement of M-AMF-DOTA (Nd)

Time-resolved fluorescence (TRF) measurements of M-AMF-DOTA(Nd) are shown in Fig. 2. Although a tailing fluorescence signal from the fluorescein moiety was detected below 850 nm in addition to the fluorescence from Nd at 880 and 900 nm in the emission spectrum without TRF measurement, the fluorescence from fluorescein was not observed in the emission spectrum with TRF measurement. Furthermore, we calculated the lifetime of Nd ion fluorescence using the equation described in the Experimental section. The calculated lifetime was 2.3 μs for the 880 nm fluorescence.

Synthesis and characterization of Avidin-AMF-DOTA(Nd)

The number of AMF-DOTA(Nd) and AMF-DOTA per avidin molecule were approximately 2.5 and 5.0, respectively.

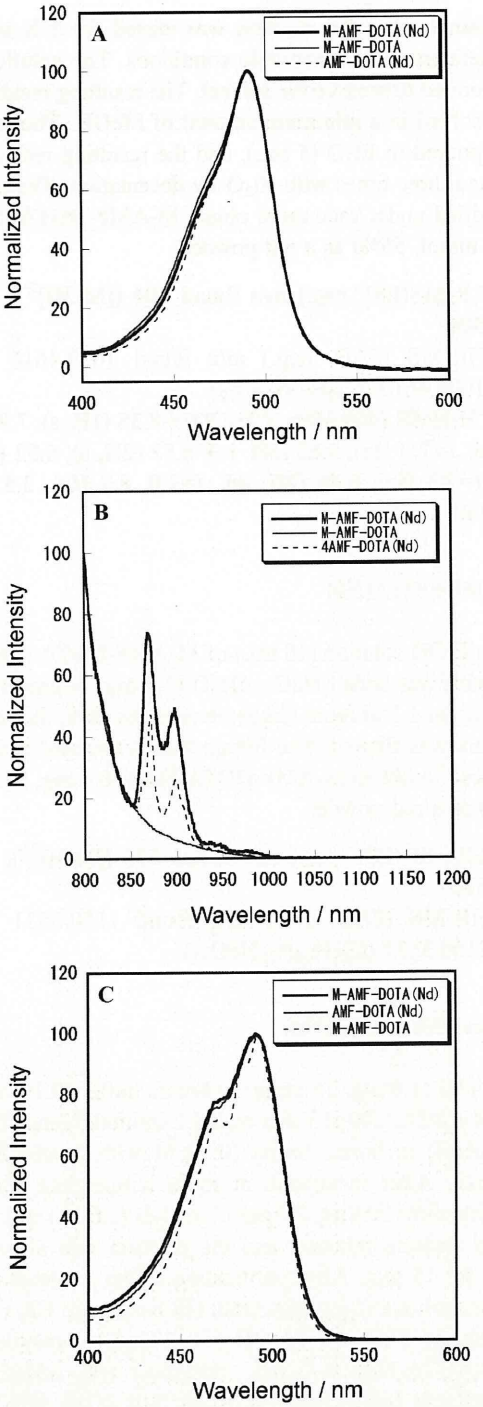

Fig. 1 Spectroscopy data for M-AMF-DOTA(Nd) (*bold line*), M-AMF-DOTA (*solid line*) and 4AMF-DOTA(Nd) (*dotted line*). **A** UV-vis absorption spectra **B** Emission spectra (λ_{ex}=488 nm). **C** Excitation spectra (λ_{em}=880 nm for M-AMF-DOTA(Nd) and 4AMF-DOTA (Nd), 515 nm for M-AMF-DOTA)

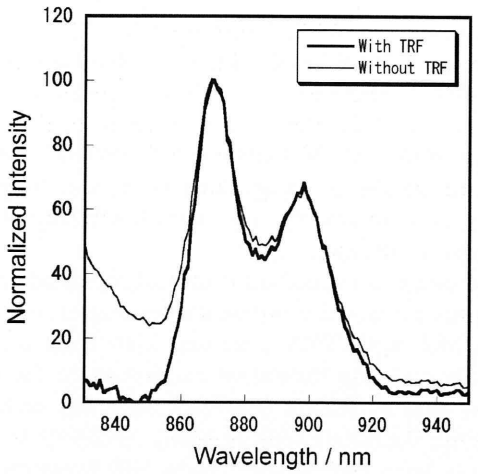

Fig. 2 Emission spectra of M-AMF-DOTA(Nd) with (*bold line*) and without (*narrow line*) time-resolved fluorescence (TRF) measurement

In the SDS-PAGE analysis of purified Avidin-AMF-DOTA(Nd), the avidin mono-subunit (17 kDa) band was clearly observed (Fig. 3). This band exhibited fluorescence in the 548~630 nm region from 302 nm excitation. The emission spectra of aqueous solutions of Avidin-AMF-DOTA(Nd) and M-AMF-DOTA(Nd) are shown in Fig. 4. Typical characteristic peaks, the same as for M-AMF-DOTA(Nd), at 880 nm and 900 nm were detected in the Avidin-AMF-DOTA(Nd) spectrum (λ_{ex}=488 nm).

Biotin binding assay of Avidin-AMF-DOTA(Nd)

The binding ability of Avidin-AMF-DOTA(Nd) to D-biotin was estimated by a displacement assay in comparison with avidin (Fig. 5). The binding of Avidin-AMF-DOTA(Nd) toward radiolabeled biotin was inhibited by D-biotin in a dose-dependent manner. Avidin-AMF-DOTA(Nd) and avidin showed similar displacement curves.

Cellular uptake study of Avidin-AMF-DOTA(Nd)

Figure 6 shows the normalized fluorescence intensity of C6 glioma cells incubated with Avidin-AMF-DOTA(Nd) and Avidin-FITC. In the cellular uptake study, Avidin-AMF-DOTA(Nd) and Avidin-FITC displayed similar time-dependent increases in fluorescence intensity after normalization by quantum yield and number of labeling agents. Cellular appearance did not change during the incubation.

Discussion

There are some requirements that an ideal fluorescent labeling agent should fulfill. First, the label needs to emit fluorescence in a region that does not overlap with other light derived from the excitation or other compounds in test tubes, solutions, organs, or cells [15,16]. A non-desired overlap could lead to a decrease in the signal-to-noise ratio. Second, fluorescence properties should not be changed by conjugation with a functional molecule for an accurate evaluation in subsequent studies. A change in the emission wavelength after conjugation would make interpretation of the data complex. Third, the ideal labeling agent should be able to label various compounds in an easy, quantifiable operation. Lastly, the fluorescent agent should not affect the chemical, physical, and biological features of the labeled compound after conjugation. The results obtained in this study indicate that M-AMF-DOTA(Nd) fulfilled all of the above requirements.

M-AMF-DOTA was easily synthesized by standard methods. For the introduction of maleimide to M-AMF-DOTA by amidation (Scheme 1, step f), the concentration of the reactants was very important. For the reaction conducted at a 10 mM concentration, only the 7-position amide M-AMF-DOTA was isolated; 4- and 10-position amide isomers were not observed. However, for reactions conducted at concentrations of 20~50 mM, 4- or 10-position isomers and di-maleimide products were observed. M-AMF-DOTA(Nd) displayed characteristic emission peaks at 880 nm and 900 nm (Fig. 1B, λ_{ex}=488 nm) which can be assigned to a typical Nd $^4F_{3/2}$ to $^4I_{9/2}$ transition, the same as 4AMF-DOTA(Nd) [5]. The quantum yield of M-AMF-DOTA(Nd) was approximately 2.5 times higher than that of 4AMF-DOTA(Nd). This might be caused

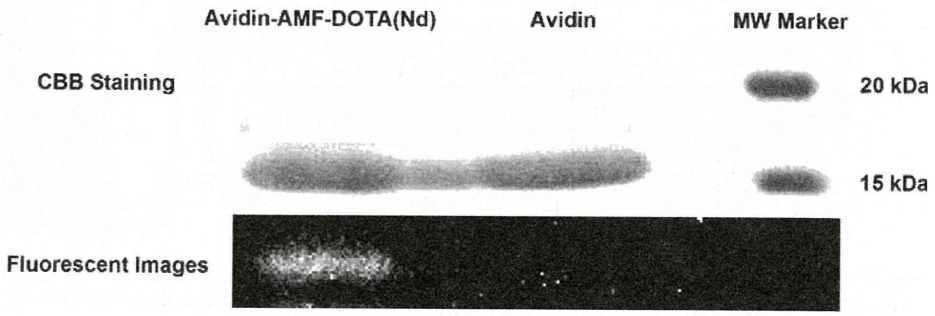

Fig. 3 CBB staining and Fluorescent images of Avidin-AMF-DOTA(Nd) and avidin

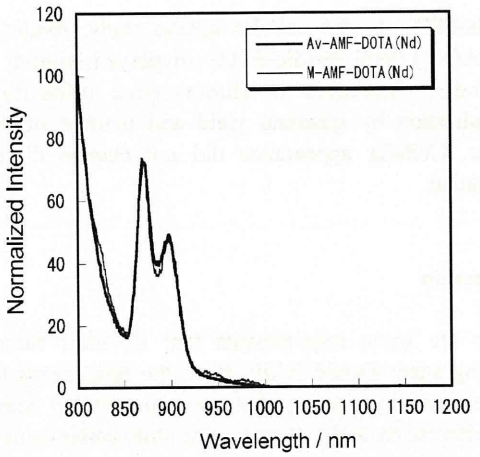

Fig. 4 Fluorescence spectra of Avidin-AMF-DOTA(Nd) (*bold line*) and M-AMF-DOTA(Nd) (*narrow line*). Each spectrum was measured with 488 nm excitation

by the DOTA modification, aminoethylation of the carboxylic acid, which hinders the approach of fluorescent quenchers (H_2O etc.) to the Nd ion in M-AMF-DOTA(Nd). In addition, the fluorescence lifetime of 2.3 μs for the Nd complex was in agreement with previous reports [17,18]. Although the fluorescence of fluorescein and the Nd ion were observed without TRF measurements, fluorescein fluorescence was not observed in the emission spectra with TRF measurement resulting in extraction of only fluorescence from Nd. Therefore, TRF measurement is a potentially useful method for compounds labeled by M-AMF-DOTA(Nd).

UV-vis spectra of buffer solutions of M-AMF-DOTA (Nd), M-AMF-DOTA and 4AMF-DOTA(Nd) showed the same absorption shape assigned to fluorescein absorption. This result suggests that the modification of DOTA and the chelation of the Nd ion to DOTA derivatives have no effect on the energy level of the fluorescein moiety. The excitation spectra of M-AMF-DOTA(Nd) (λ_{em}=880 nm) and M-AMF-DOTA (λ_{em}=515 nm) showed much the same features (Fig. 1C). Thus, the supposition that the luorescence of M-AMF-DOTA(Nd) at 880~900 nm is derived from the transfer of energy from an excited fluorescein moiety, the same as in the case of 4AMF-DOTA(Nd) [5], is supported by the data.

NIR fluorescence analysis is particularly suited to living organisms because they contain few fluorescent compounds in the NIR region (700~1000 nm) while there are many naturally occurring fluorescent compounds in the visible region, such as fluorite (400~600 nm) [19], anthracene (400 nm), chlorophyll (680 nm) [20], NAD(P)H (450 nm) [21] and flavin (520 nm) [22]. Thus, NIR fluorescent dyes are recognized to be useful for fluorescent analysis [23–25]. In addition, fluorescence from lanthanides has a significant advantage in that the wavelength is constant with changes in environmental factors (solvent, pH, etc,) [6]. This is derived from the mechanism of lanthanide fluorescence where the 4f orbital responsible for fluorescence is located inside the 5 s and 5 d orbitals, which protect the fluorescence from environmental effects. A very large Stoke's shift for M-AMF-DOTA(Nd) (about 400 nm) is another advantage over most other organic fluorescent labels. This contributes to the easy separation of the emission signals from the excitation light by suitable optical filters. Although to date there are few instruments with good imaging ability in the NIR region (especially 800~1200 nm), NIR fluorescent analysis using potential labeling agents such as M-AMF-DOTA(Nd) could be effective with the development of suitable imaging instruments.

Thiolated avidin was easily labeled by M-AMF-DOTA (Nd). The number of AMF-DOTA(Nd) complexes per avidin was half that of AMF-DOTA under the same

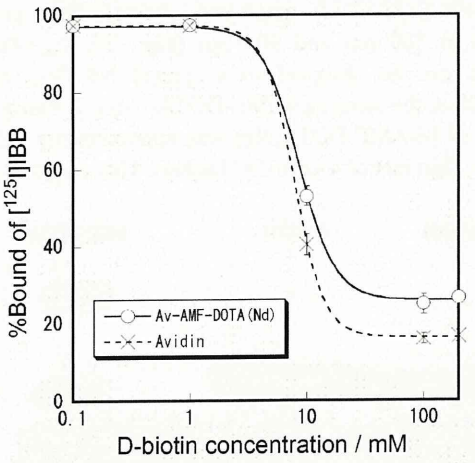

Fig. 5 Displacement assay of Avidin-AMF-DOTA(Nd) (*solid line*) (or avidin (*dotted line*)), [^{125}I]-IBB and various concentrations of D-biotin

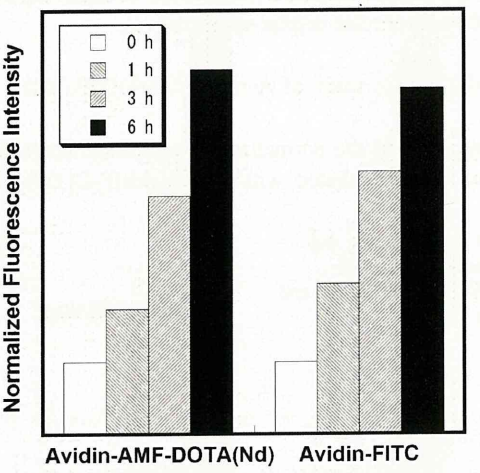

Fig. 6 Normalized fluorescence intensity of C6 glioma cells incubated with Avidin-AMF-DOTA(Nd) (*left*) or Avidin-FITC (*right*)

reaction conditions, which would seem to be caused by a difference in tertiary structure. It is well known that lanthanide-DOTA derivative complexes form cage-like structures [26–28]. Therefore, M-AMF-DOTA(Nd) is a more rigid and hindered structure compared with M-AMF-DOTA. Thus, the maleimide group of M-AMF-DOTA(Nd) as compared with M-AMF-DOTA would have less chance of approaching a thiol group. It is remarkable that M-AMF-DOTA(Nd) is still reactive enough for the following studies as shown in Figs. 3, 4, 5, and 6.

Since maleimides readily react with thiols, we labeled avidin through Lys side chain NH_2 groups via conversion to thiols by reaction with 2-iminothiolane. This intermediate step is necessary because all Cys side chains in avidin form disulfide bonds [29] while most of the Lys side chains (about 6 or 7 per avidin monomer) are free on the protein surface [29]. The labeling reaction was easily completed, which demonstrates that the M-AMF-DOTA(Nd) fluorescent labeling agent could be linked with proteins through not only thiol but also primary amine side chains.

In a displacement assay, both Avidin-AMF-DOTA(Nd) and naive avidin were inhibited by D-biotin in a similar dose-dependent manner (Fig. 5). This result suggests that the conjugation did not affect the recognition ability of avidin with D-biotin. Another biological characteristic of avidin is its internalization into tumor cells after recognition by lectins expressed on the tumor cell surface [30, 31]. The flow cytometry analysis of C6 glioma cells after incubation with Avidin-AMF-DOTA(Nd) or Avidin-FITC displayed similar time-dependent increases in fluorescence intensity (Fig. 6). Avidin-FITC has been used as an effective fluorescent labeled avidin in evaluating receptor mediated endocytosis in *in vitro* studies [32]. Although FITC is a very good labeling agent that emits bright (ϕ=0.60) fluorescence, it is not applicable for *in vivo* studies because of its visible (λ_{em}=515 nm) fluorescence. On the other hand, M-AMF-DOTA(Nd) is potentially usable for *in vivo* fluorescence imaging because of its NIR fluorescence as described above.

For the spacer between the fluorophore and avidin, the results indicate that conjugation did not disrupt the fluorescent properties (Fig. 4) or the distinctive binding features of avidin (Figs. 5 and 6) and support the validity of the spacer selection.

Although the data are not shown, M-AMF-DOTA(Nd) could not be used for fluorescent analysis under strongly acidic conditions (lower than pH 5) because the fluorescent signal disappeared, a property that depends on the particular fluorescein used as the antenna moiety of M-AMF-DOTA (Nd) [5, 6]. We recently reported another NIR fluorescent compound with a large Stoke's shift, PAN-DOTA(Yb), had constant fluorescent features over a wide pH range (3~11) [6]. Application of the findings obtained in this study to PAN-DOTA(Yb) may lead to the development of an even more useful NIR fluorescent labeling agent in the future.

Conclusion

In this study, we synthesized an M-AMF-DOTA(Nd) derivative that includes maleimide linker and NIR fluorophore moieties as a new labeling agent with a large Stoke's shift. M-AMF-DOTA(Nd) was used to easily label an avidin molecule through Lys side chains without loss of functional characteristics of avidin or fluorescent features of the labeling agent. The results indicate that M-AMF-DOTA (Nd) is a potential labeling agent for routine fluorescence analysis with several favorable properties including NIR emission, constant fluorescence unaffected by conjugation, good labeling ability for amines and thiols, and no effect on the chemistry or biology of the labeled protein.

References

1. Kraig E, Sheetz JS (2009) Ultrafast optics: Imaging and manipulating biological systems. J Appl Phys 105:051101
2. El-Deiry WS, Sigman CC, Kelloff GJ (2006) Imaging and oncologic drug development. J Clin Oncol 24(20):3261–3273
3. Uversky VN (2007) Nanoimaging in protein-misfolding and -conformational diseases. Nanomed 2(5):615–643
4. Sukhanova A, Nabiev I (2008) Fluorescent nanocrystal-encoded microbeads for multiplexed cancer imaging and diagnosis. Crit Rev Oncol Hematol 68(1):39–59
5. Aita K et al (2007) Development of a novel neodymium compound for in vivo fluorescence imaging. Luminescence 22 (5):455–461
6. Aita, K., et al., (2009), NIR fluorescent ytterbium compound for in vivo fluorescence molecular imaging. Luminescence, in press.
7. Woods M, Sherry AD (2003) Synthesis and luminescence studies of aryl substituted tetraamide complexes of europium(III): a new approach to pH responsive luminescent europium probes. Inorg Chem 42(14):4401–4408
8. Baffreau J et al (2008) Fullerene C60-perylene-3, 4:9, 10-bis (dicarboximide) light-harvesting dyads: spacer-length and bay-substituent effects on intramolecular singlet and triplet energy transfer. Chemistry 14(16):4974–4992
9. Zhu Z et al (1994) Directly labeled DNA probes using fluorescent nucleotides with different length linkers. Nucleic Acids Res 22 (16):3418–3422
10. Bruschi M et al (2009) New iodo-acetamido cyanines for labeling cysteine thiol residues. A strategy for evaluating plasma proteins and their oxido-redox status. Proteomics 9(2):460–469
11. Kuwabara T et al (2006) Host-guest complexation affected by pH and length of spacer for hydroxyazobenzene-modified cyclodextrins. J Phys Chem A 110(50):13521–13529
12. Kuramitz H et al (2008) Simultaneous multiselective spectroelectrochemical sensing of the interaction between protein and its ligand using the redox dye nile blue as a label. Anal Chem 80 (24):9642–9648
13. Zhang J et al (2005) Sensitization of near-infrared-emitting lanthanide cations in solution by tropolonate ligands. Angew Chem Int Ed Engl 44(17):2508–2512

14. Kudo T, et al. (2009) Imaging of HIF-1-active tumor hypoxia using a protein effectively delivered to and specifically stabilized in HIF-1-active tumor cells. J Nucl Med, in press
15. Francis-Sedlak ME et al (2009) Characterization of type I collagen gels modified by glycation. Biomaterials 30(9):1851–1856
16. Zheng W et al (2008) Autofluorescence of epithelial tissue: single-photon versus two-photon excitation. J Biomed Opt 13(5):054010
17. Bassett AP et al (2004) Highly luminescent, triple- and quadruple-stranded, dinuclear Eu, Nd, and Sm(III) lanthanide complexes based on bis-diketonate ligands. J Am Chem Soc 126(30):9413–9424
18. Hasegawa Y et al (2000) Luminescence of novel neodymium sulfonylaminate complexes in organic media. Angew Chem Int Ed Engl 39(2):357–360
19. Gaft M et al (2008) Time-resolved laser-induced luminescence of UV-vis emission of Nd3+ in fluorite, scheelite and barite. J Alloys Compd 451(1–2):56–61
20. Hense BA et al (2008) Use of fluorescence information for automated phytoplankton investigation by image analysis. J Plankton Res 30(5):587–606
21. Brennan AM, Connor JA, Shuttleworth CW (2007) Modulation of the amplitude of NAD(P)H fluorescence transients after synaptic stimulation. J Neurosci Res 85(15):3233–3243
22. Kosterin P et al (2005) Changes in FAD and NADH fluorescence in neurosecretory terminals are triggered by calcium entry and by ADP production. J Membr Biol 208(2):113–124
23. Chen X, Conti PS, Moats RA (2004) In vivo near-infrared fluorescence imaging of integrin alphavbeta3 in brain tumor xenografts. Cancer Res 64(21):8009–8014
24. Hansch A et al (2004) In vivo imaging of experimental arthritis with near-infrared fluorescence. Arthritis Rheum 50(3):961–967
25. Mizukami S et al (1999) Imaging of caspase-3 activation in HeLa cells stimulated with etoposide using a novel fluorescent probe. FEBS Lett 453(3):356–360
26. Quici S et al (2004) New lanthanide complexes for sensitized visible and near-IR light emission: synthesis, 1H NMR, and X-ray structural investigation and photophysical properties. Inorg Chem 43(4):1294–1301
27. Zucchi G et al (2002) Highly luminescent, visible-emitting lanthanide macrocyclic chelates stable in water and derived from the cyclen framework. Inorg Chem 41(9):2459–2465
28. Amin S et al (1995) Laser-induced luminescence studies and crystal-structure of the europium(Iii) complex of 1, 4, 7, 10-tetrakis(carbamoylmethyl)-1, 4, 7, 10-tetraazacyclododecane - the link between phosphate diester binding and catalysis by lanthanide(Iii) macrocyclic complexes. Inorg Chem 34 (12):3294–3300
29. Livnah O et al (1993) Three-dimensional structures of avidin and the avidin-biotin complex. Proc Natl Acad Sci U S A 90 (11):5076–5080
30. Yao Z et al (1998) Avidin targeting of intraperitoneal tumor xenografts. J Natl Cancer Inst 90(1):25–29
31. Yao Z et al (1998) Imaging of intraperitoneal tumors with technetium-99 m GSA. Ann Nucl Med 12(2):115–118
32. Ouchi T et al (2004) Design of attachment type of drug delivery system by complex formation of avidin with biotinyl drug model and biotinyl saccharide. J Control Release 94(2–3):281–291

Research Article

LUMINESCENCE
The Journal of Biological and Chemical Luminescence

Received: 22 October 2008, Revised: 19 February 2009, Accepted: 1 February 2009 Published online in Wiley Interscience: 29 May 2009

(www.interscience.wiley.com) DOI 10.1002/bio.1136

NIR fluorescent ytterbium compound for *in vivo* fluorescence molecular imaging

Kazuki Aita[a,b], Takashi Temma[a], Yuji Kuge[a,c], Koh-ichi Seki[b] and Hideo Saji[a]*

ABSTRACT: We have developed a new NIR fluorescent probe based on an ytterbium(III) (*E*)-1-(pyridin-2-yl-diazenyl)naphthalen-2-ol (PAN) complex. This probe emits near-infrared luminescence derived from the Yb ion through excitation of the PAN moiety with visible light (λ_{ex} = 530 nm, λ_{em} = 975 nm). The results support the possible utility of the probe for *in vivo* fluorescence molecular imaging. Copyright © 2009 John Wiley & Sons, Ltd.

Keywords: ytterbium; near-infrared; energy transfer; fluorescence

Introduction

Molecular imaging is a rapidly emerging biomedical research field that may be defined as the visual representation, characterization and quantification of biological processes at the cellular and subcellular levels within a living organism.[1–3] As a molecular imaging technique, fluorescence imaging has attracted great interest, stimulating the development of more effective probes.

A potential probe for *in vivo* fluorescence imaging should emit light in the near-infrared (NIR) region (700–1000 nm). NIR light can permeate the body without intense absorbance or scatter by tissues,[4] and there is negligible self-fluorescence in the NIR region from living systems. In addition, a potential fluorescent probe should possess a large Stoke's shift to increase the signal-to-noise ratio. Provided that the Stoke's shift is large enough, scattered and reflected light derived from excitation light could be eliminated by appropriate filters. However, to the best of our knowledge, there are few reports of probes that fulfill the criteria of NIR fluorescence emission with a large Stoke's shift.

Some lanthanide (e.g. Eu, Tb, Nd, Yb, and Er) complexes that include an antenna moiety, a sensitizing chromophore, are well known as good fluorophores.[5–8] Their useful emission features, such as a large Stoke's shift (over 10 times larger than typical fluorescent dyes) and element-specific emission wavelength (visible in the IR region), have the potential for fluorescence imaging. Nd and Yb ions are especially suited for *in vivo* fluorescence imaging because of their NIR luminescence originating from $^4F_{3/2}$ to $^4I_{9/2}$ (at 870 nm) and $^2F_{5/2}$ to $^2F_{7/2}$ (at 975 nm) transitions, respectively.[9–11]

For these reasons, we aimed to develop a new fluorescent probe containing an ytterbium complex (Scheme 1). As a chelating moiety, 1,4,7,10-tetraazacyclododecane-1,4,7,10-tetraacetic acid (DOTA) was selected because DOTA and Yb^{3+} ion form a highly stable complex (the log K value of Yb^{3+} and $DOTA^{4-}$ is 25.81[12]) due to the tight coordination of DOTA with up to eight coordination sites. This implies that the complex would not be susceptible to metabolic degradation in living systems.[6] As an antenna moiety, (*E*)-1-(pyridin-2-yl-diazenyl)naphthalen-2-ol (PAN) was selected for three reasons. First, it is well known that PAN absorbs blue-green light (around 500 nm), which is harmless to living systems and reasonable for Yb excitation. Second, PAN is not fluorescent and has negligible fluorescence in the red to NIR region. Finally, the PAN structure does not contain pH-sensitive groups (carboxylic acid, primary amine, etc.). It was expected that a probe with these characteristics would display a high fluorescence yield and high *in vivo* stability.

In this study, we have synthesized PAN–DOTA(Yb), which includes the Yb–DOTA complex and PAN as a NIR fluorescent probe (Scheme 1), and have investigated its chemical and physical properties.

Materials and methods

Materials

All chemicals used in this study were commercial products of the highest purity and were further purified by standard methods, if necessary.

Instruments

FT-IR spectra were recorded with a Jasco FT/IR-4100 (Nihon Bunko Inc., Tokyo, Japan). UV–vis spectra were measured using a Hitachi U2001 (Hitachi High-Tech Manufacturing and Service Corporation, Ibaraki, Japan). ESI-MS measurements were performed on a Shimadzu LC-MS2010 EV (Shimadzu Corporation, Kyoto, Japan). ^{1}H-NMR spectra were recorded on a Jeol JNM-AL400 (Jeol Ltd, Tokyo, Japan). Fluorescence spectroscopy and quantum yield analysis were performed with a Fluorolog-3 (Horiba Jobin Yvon Inc., Kyoto, Japan). The slit width was 10 nm for both excitation and emission measurements.

* Correspondence to: H. Saji, Department of Patho-Functional Bioanalysis, Graduate School of Pharmaceutical Sciences, Kyoto University, Japan. E-mail: hsaji@pharm.kyoto-u.ac.jp

[a] Department of Patho-Functional Bioanalysis, Graduate School of Pharmaceutical Sciences, Kyoto University, Japan

[b] Central Institute of Isotope Science, Hokkaido University, Japan

[c] Department of Tracer Kinetics and Bioanalysis, Graduate school of Medicine, Hokkaido University, Japan

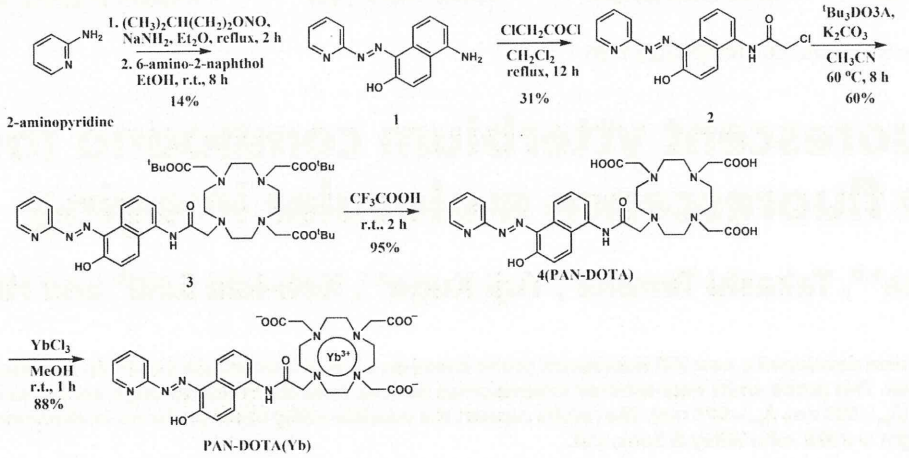

Scheme 1. Synthetic scheme for PAN-DOTA(Yb).

Fluorescence emission and excitation spectral measurements

The fluorescence emission spectra of PAN-DOTA(Yb) (10 μM) were measured in 10 mM Tris–HCl buffer (pH 8.0), 10 mM Britton–Robinson's buffer (pH 2.0–11.0), MeOH, EtOH and DMSO [each organic solvent contained 0.1% (v/v) Et_3N] at 25°C, following excitation at 530 nm. Excitation spectra were obtained at an emission wavelength of 975 nm.

Quantum yield analysis

The quantum yield analyses of PAN–DOTA(Yb) were measured by a previously reported method[13] in 10 mM Tris–HCl buffer (pH 8.0), MeOH, EtOH and DMSO [each organic solvent contained 0.1% (v/v) Et_3N] at 25°C, following excitation at 530 nm and emission at 975 nm. The reference compound [Yb(Tropolonate)$_4$] was measured at 380 nm excitation and 975 nm emission in 10 mM Tris–HCl buffer. The absorbance of the samples was adjusted to not exceed 0.2 at the excitation wavelength. The wavelength dependence of excitation light intensity and the detection efficiency of emission light were as given from Horiba Jobin Yvon Inc.

UV–visible absorption spectral measurements

The absorption spectral changes of PAN–DOTA and PAN–DOTA(Yb) (10 μM) in 10 mM Tris–HCl buffer (pH 8.0) at 25°C were determined.

Synthesis

(*E*)-1-(pyridin-2-yl-diazenyl)-5-amino-naphthalen-2-ol (PAN–NH_2). To a solution of 2-amino-pyridine (940 mg, 10.0 mmol) in dry THF (50 mL) was added sodium amide (390 mg, 10.0 mmol) under a slight flow of nitrogen gas. Vigorous stirring was maintained at 40°C. After ammonia evolution had ceased, isopentylnitrate (1.01 g, 10.0 mmol) was added and stirring was continued for another hour under a nitrogen atmosphere at 40°C. The precipitated sodium diazotate was filtered, washed with Et_2O and immediately dissolved in cold, dry THF (30 mL). The THF solution of sodium diazotate was added to a solution of 5-amino-2-naphthol (1.59 g, 10.0 mmol) in THF (30 mL), and with carbon dioxide gas bubbling. The resulting solution was concentrated by evaporation. PAN–NH_2 was isolated by silica gel column chromatography (diameter = 3 cm, column length = 20 cm, eluent $CHCl_3$:MeOH = 10:1). The desired fractions were collected and concentrated by evaporation. The resulting powder was dried under vacuum to obtain PAN–NH_2 (370 mg, 1.4 mmol, 14%) as a reddish brown powder.

MS (ESI, pos.) *m/z* found 265 ([M + H]$^+$), calcd 265 ^{1}H-NMR (400 MHz, CD_3OD) δ 8.55 (1H, d, J = 1.0 Hz), 8.27 (1H, d, J = 1.0 Hz), 8.05 (1H, d, J = 8.6 Hz), 7.97–7.86 (2H, m), 7.74 (1H, d, J = 9.0 Hz), 7.38–7.34 (1H, m), 7.02 (1H, t, J = 10.5 Hz), 6.61 (1H, d, J = 8.8 Hz).

(*E*)-1-(pyridin-2-yl-diazenyl)-5-amidochloromethyl-naphthalen-2-ol (PAN–Cl). PAN–NH_2 (528 mg, 2.0 mmol) was dissolved in dry THF (20 mL). To the solution was added a solution of $ClCH_2COCl$ (250 mg, 2.2 mmol) dissolved in dry THF (10 mL), causing the solution to become black. The mixture was stirred for 5 h at room temperature and then concentrated by evaporation. PAN–Cl was isolated by silica gel column chromatography (diameter = 3 cm, column length = 20 cm, eluent $CHCl_3$:MeOH = 10:1). The desired fractions were collected and concentrated by evaporation. The resulting powder was dried under vacuum to obtain PAN–Cl (211 mg, 0.6 mmol, 31%) as a yellow powder.

MS (ESI, pos.) *m/z* found 341 ([M + H]$^+$), calcd 341. ^{1}H-NMR (400 MHz, CD_3OD) δ 8.56 (1H, ddd, J = 0.9, 1.9, 4.9 Hz), 8.27 (1H, d, J = 2.6 Hz), 8.06 (1H, d, J = 8.7 Hz), 7.99–7.94 (2H, m), 7.88 (1H, td, J = 1.3, 8.0 Hz), 7.37 (1H, ddd, J = 1.1, 5.2, 7.4 Hz), 7.04 (1H, dd, J = 2.6, 9.1 Hz), 6.63 (1H, d, J = 8.7 Hz), 4.15 (2H, s).

1-[(*E*)-1-(pyridin-2-yl-diazenyl)-5-amidomethyl-naphthalen-2-ol]-1,4,7,10-tetraazacyclododecane-4,7,10-triacetic acid tri-*tert*-butyl ester (PAN-^{t}Bu$_3$DOTA). A dry DMF suspension (10 mL) of 1,4,7,10-tetraazacyclododecane-1,4,7-triacetic acid tri-*tert*-butyl ester (^{t}Bu$_3$DO3A) (51.5 mg, 0.1 mmol), K_2CO_3 (138 mg, 1.0 mmol) and KI (166 mg, 1.0 mmol) was stirred for 5 min at 60°C under anaerobic conditions. To the suspension was then slowly added a solution of PAN–Cl (34.0 mg, 0.1 mmol) in dry DMF (10 mL). After stirring for 13 h at 60°C, the suspension was filtered and the residue was washed with MeCN. This residue was added to MeOH (20 mL), stirred for 30 min to give a reddish suspension which was filtered and washed with MeOH. The filtrate was

LUMINESCENCE
The Journal of Biological and Chemical Luminescence

concentrated by evaporation. PAN–^{t}Bu$_3$DOTA was isolated by silica gel column chromatography (diameter = 1.5 cm, column length = 15 cm, eluent $CHCl_3$:MeOH = 10:1). The desired fractions were collected and concentrated by evaporation. The resulting powder was dried under vacuum to obtain PAN–^{t}Bu$_3$DOTA (49.0 mg, 60 μmol, 60%) as a red powder.

MS (ESI, pos.) *m/z* found 819 ([M + H]$^+$), calcd 819. ^{1}H-NMR (400 MHz, $CDCl_3$) δ 8.27 (1H, dd, *J* = 3.3, 8.3 Hz), 7.65 (1H, d, *J* = 8.5 Hz), 7.56 (1H, d, J = 7.4 Hz), 7.43 (1H, d, *J* = 7.9 Hz), 7.36-7.23 (4H, m), 6.66 (1H, d, J = 9.9 Hz), 3.82 (6H, s), 3.71 (2H, s), 3.32–2.79 (16H, br), 1.43 (27H, s).

1-[(*E*)-1-(pyridin-2-yl-diazenyl)-5-amidomethyl-naphthalen-2-ol]-1,4,7,10-tetraazacyclododecane-4,7,10-triacetic acid (PAN–DOTA). PAN–^{t}Bu$_3$DOTA (41.0 mg, 50 μmol) was dissolved in trifluoroacetic acid (5.0 mL) at 0°C. After stirring for 1 h at 0°C, the resulting solution was poured into Et_2O (50 mL), and filtered. The residue was washed with Et_2O three times, and the resulting powder was dried under vacuum to obtain PAN–DOTA (30.8 mg, 48 μmol, 95%) as a reddish yellow powder.

MS (ESI, neg.) *m/z* found 649 ([M – H]$^-$), calcd 649. ^{1}H-NMR (400 MHz, CD_3OD) δ 7.94 (1H, d, *J* = 7.9 Hz), 7.61 (1H, d, *J* = 7.1 Hz), 7.49 (1H, d, J = 8.7 Hz), 7.34 (2H, t, *J* = 7.9 Hz), 7.25 (1H, t, *J* = 7.9 Hz), 7.12-7.10 (3H, m), 3.92 (8H, br), 3.20–3.04 (16H, br).

PAN–DOTA(Yb)

To an MeOH solution (2 mL) containing PAN–DOTA (6.5 mg, 10 μmol) was added $YbCl_3$ $6H_2O$ (3.9 mg, 10 μmol) in MeOH solution (2 mL). After stirring for 1 h at room temperature, the resulting solution was poured into Et_2O (10 mL), and filtered. The residue was washed with Et_2O three times, and the resulting powder was dried under vacuum to obtain PAN–DOTA(Yb) (7.2 mg, 8.8 μmol, 88%) as a red powder. MS(ESI, pos.) *m/z* found 822 ([M – H]$^-$), calcd. 822.

Results

Synthesis of PAN–DOTA(Yb)

PAN–DOTA was synthesized from 2-aminopyridine in four steps, as shown in Scheme 1, and the overall yield from starting material was 2.5%. PAN–DOTA(Yb) was synthesized by stirring PAN–DOTA and $YbCl_3$ in MeOH with the yield of 88%. Other lanthanide complexes, PAN–DOTA(Ln) (Ln = Eu, Tb and Nd), were similarly prepared from $EuCl_3$, $TbCl_3$ and $NdCl_3$ with the yields of 90, 85 and 92%, respectively.

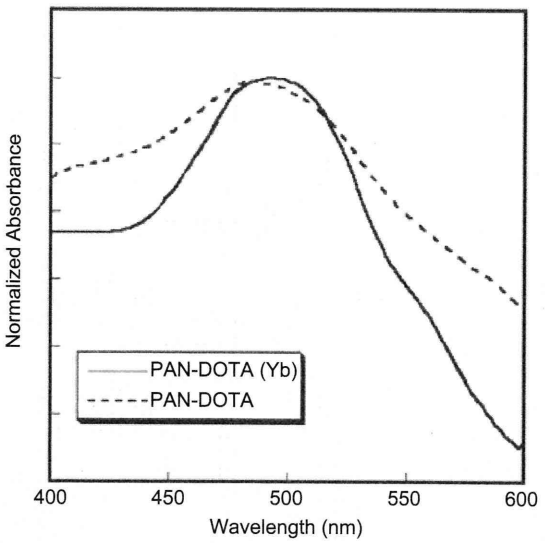

Figure 1. UV-vis absorption spectra of PAN-DOTA (dotted line) and PAN-DOTA(Yb) (solid line).

Spectroscopic characterizations of PAN–DOTA(Yb) in aqueous solution

In the IR spectra, carbonyl C=O stretching absorptions were observed at 1732 cm^{-1} for PAN–DOTA and 1717 cm^{-1} for PAN–DOTA(Yb), and amide N–H bending absorptions were found at 1569 cm^{-1} for PAN–DOTA and 1559 cm^{-1} for PAN–DOTA(Yb) (data not shown).

UV–vis spectra of aqueous solutions of PAN–DOTA(Yb) and PAN–DOTA are shown in Fig. 1. The maximal absorption wavelengths were 490 nm [PAN–DOTA(Yb)] and 480 nm (PAN–DOTA), respectively.

The emission spectra of aqueous solutions of PAN–DOTA(Yb), PAN–DOTA, $YbCl_3$ and DOTA(Yb) are shown in Fig. 2(A). A sharp and strong peak at 975 nm was detected only in the PAN–DOTA(Yb) spectrum (λ_{ex} = 530 nm). In contrast, no fluorescence

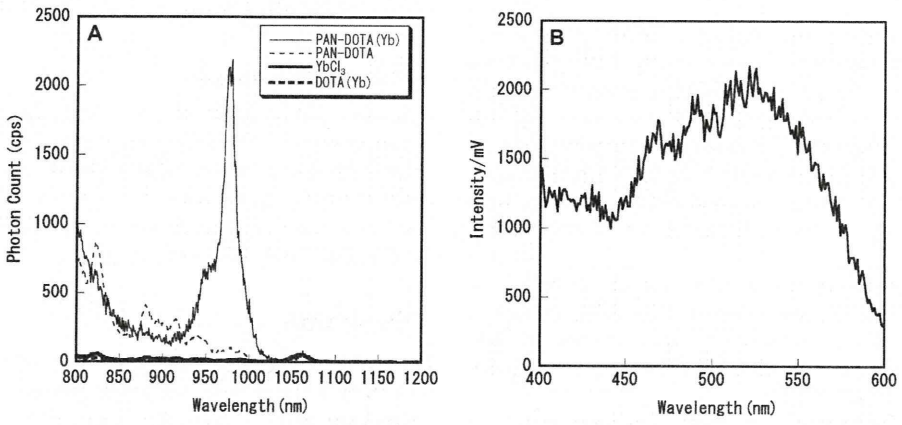

Figure 2. Spectroscopy data for PAN-DOTA (dotted line), PAN-DOTA(Yb) (solid line), $YbCl_3$ (solid and bold line) and DOTA(Yb) (dotted and bold line). (A) Emission spectra (λ_{ex} = 530 nm). (B) Excitation spectra (λ_{em} = 975 nm).

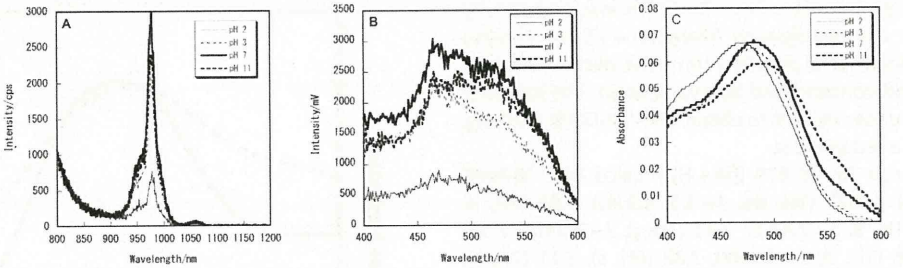

Figure 3. pH effect on spectral features of PAN-DOTA(Yb). (A) Emission spectra (λ_{ex} = 530 nm). (B) Excitation spectra (λ_{em} = 975 nm). (C) UV-vis absorption spectra. Spectra show the results at pH 2.0 (solid line), pH 3.0 (dotted line), pH 7.0 (solid and bold line) and pH 11.0 (dotted and bold line).

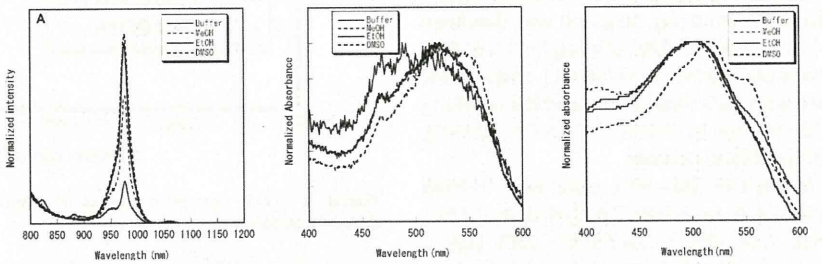

Figure 4. Solvent effects on spectral features of PAN-DOTA(Yb). (A) Emission spectra (λ_{ex} = 530 nm). (B) Excitation spectra (λ_{em} = 975 nm). (C) UV-vis absorption spectra. Spectra were measured in buffer (solid line), MeOH (dotted line), EtOH (solid and bold line) and DMSO (dotted and bold line).

peak was detected for PAN–DOTA, $YbCl_3$ or DOTA(Yb) under the same conditions.

Figure 2(B) shows the excitation spectrum of an aqueous solution of PAN–DOTA(Yb) (λ_{em} = 975 nm). The wavelength maxima was at 530 nm while an overtone of the detection light somewhat affected the shape of the curve around 490 nm.

PAN–DOTA complexes with other lanthanides gave differing fluorescence spectra. PAN–DOTA(Nd) showed a small peak at approximately 880 nm due to a typical neodymium $^4F_{3/2}$ to $^4I_{9/2}$ transition upon excitation with 530 nm light. PAN–DOTA(Eu) and PAN–DOTA(Tb) had no emission peaks from excitation at 530 nm in part because of the higher energy levels required to excite Eu and Tb.

Effects of pH and solvent on the fluorescence of PAN–DOTA(Yb)

The effect of pH on the fluorescence of PAN–DOTA(Yb) was examined [Fig. 3(A)]. The fluorescence intensity of PAN–DOTA(Yb) remained constant in the pH 3–11 range; however, it was weak at pH 2. Similarly, the excitation spectra [Fig. 3(B)] and the UV–vis absorption spectra [Fig. 3(C)] also showed that the energy levels of PAN–DOTA(Yb) were almost constant from pH 3 to 11. In addition, in the pH 2–11 range, no degradation products were detected by electrospray ionization mass spectrometry (ESI-MS) analysis.

PAN–DOTA(Yb) could be dissolved in several polar organic solvents. Figure 4 shows the emission [Fig. 4(A)], excitation [Fig. 4(B)] and UV–vis absorption [Fig. 4(C)] spectra of PAN–DOTA(Yb) in 10 mM Tris–HCl buffer (pH 8.0) and the organic solvents MeOH, EtOH and DMSO.

The λ_{max} of the excitation wavelength that gives a 975 nm emission changed slightly around 520 nm in the three tested organic solvents [Fig. 4(B)]. On the other hand, the emission spectra showed the exact same λ_{max} in the four tested solvents while the fluorescence intensity changed [Fig. 4(A)].

Table 1. Quantum yields of PAN–DOTA(Yb) and $[Yb(tropolonate)_4]^-$

Complex	Solvent	Quantum yield
PAN–DOTA(Yb)	0.01 M Tris buffer (pH 8.0)	8.6×10^{-5}
PAN–DOTA(Yb)	MeOH[a]	1.8×10^{-4}
PAN–DOTA(Yb)	EtOH[a]	3.5×10^{-4}
PAN–DOTA(Yb)	DMSO[a]	5.4×10^{-4}
$[Yb(Tropolonate)_4]^-$	0.01 M Tris buffer (pH 8.0)	2.4×10^{-4}[b]

[a]Contains 0.1% (v/v) Et_3N.
[b]This value is from Zhang *et al.*[13]

Quantum yield analysis

Quantum yields (Φ) of PAN–DOTA(Yb) were measured in several solvents using $[Yb(Tropolonate)_4]^-$ ($\Phi = 2.4 \times 10^{-4}$ in 0.01 M TRIS buffer[13]) as a standard. Table 1 shows the quantum yields of PAN–DOTA(Yb) to be 8.6×10^{-5}, 1.8×10^{-4}, 3.5×10^{-4} and 5.4×10^{-4} as measured at room temperature in Tris buffer (pH 8.0), MeOH, EtOH and DMSO, respectively.

Discussion

In IR spectra, the peak shifts with the Yb chelation suggest that the three carbonyl and one amide groups of the DOTA moiety participate in chelation of the Yb ion. In UV–vis absorption spectra (Fig. 1), the wavelength maxima changed slightly after metal chelation. Since it was previously reported that the maximal